In presenting this thesis in partial fulfillment of the requirements for an advanced degree at Idaho State University, I agree that the Library shall make it freely available for inspection. I further state that permission for extensive copying of my thesis for scholarly purposes may be granted by the Dean of the Graduate School, Dean of my academic division, or by the University Librarian. It is understood that any copying or publication of this thesis for financial gain shall not be allowed without my written permission.

Signature‗‗‗‗‗‗‗‗‗‗‗‗‗‗‗‗‗‗‗‗‗‗‗

Date‗‗‗‗‗‗‗‗‗‗‗‗‗‗‗‗‗‗‗‗‗‗‗‗‗

A MEASUREMENT OF SEMI INCLUSIVE DEEP INELASTIC
SCATTERING PION ASYMMETRIES TO TEST INDEPENDENT
FRAGMENTATION

by

Tamar Didberidze

A dissertation

submitted in partial fulfillment

of the requirements for the degree of

Doctor of Philosophy in the Department of Physics

Idaho State University

Fall 2012

To the Graduate Faculty:

The members of the committee appointed to examine the dissertation of Tamar Didberidze find it satisfactory and recommend that it be accepted.

_____
Dr. Tony A. Forest,
Major Advisor

_____
Dr. Dustin E. McNulty,
Committee Member

_____
Dr. Mahbub Khandaker,
Chairman of Department

_____
Dr. Steven L. Shropshire,
Committee Member

_____
Dr. Daniel S. Dale,
Committee Member

_____
Dr. Robert J. Fisher,
Graduate Faculty
Representative

Acknowledgments

I am thankful to my advisor Dr. Tony Forest for the professional expertise that I have gained in experimental physics and for helping me to finish my degree. I would also like to thank all my former professors and fellow students in the lab working with me. I wish to thank Sandra O'Neill for making sure that everything goes smoothly in the department; without her we would be lost. I would also like to thank my PhD committee members for their time and patience.

I would like to thank my friends and my family for all their support that they have given me. Especially, my husband Brian for his patience, and my son Pascal for always putting a smile on my face. I thank my aunt Madona for her constant and boundless support. I thank my brother Temuri for being there for my grandparents. And at last, I would like to thank the Mother Nature for all the mountains, Pink Floyd for great music and Outdoor Adventure Center at Idaho State University for their experiences.

Table of Contents

List of Figures

List of Tables

Abstract

Semi-inclusive deep inelastic scattering (SIDIS) experiments may be used to identify the flavor of the quark that participates in the scattering process. Semi-inclusive scattering is defined as an electron scattering experiment in which the scattered electron and one hadron are detected in the final state. Experiments at Jefferson Lab have used longitudinally polarized electron beams to probe longitudinally polarized Hydrogen (^{15}NH$_3$) and Deuterium (^{15}ND$_3$) targets to investigate the quark's contribution to the properties of a nucleon. This thesis reports a measurement of SIDIS pion asymmetries using the CEBAF Large Acceptance Spectrometer (CLAS) at Thomas Jefferson National Laboratory. The incident electron's energy was 4.2 GeV and covered a kinematic region where the struck quark carries at least 30% of the nucleons total momentum ($x_B \geq 0.3$). The electrons scatter mostly from valence quarks in this kinematic region allowing measurements which are less sensitive to the ocean of quark-antiquark pairs that are also inside a nucleon.

CHAPTER 1

Theory

Understanding the spin structure of a nucleon remains a major challenge for hadronic physics. The parton model predicted that quarks carry about $(67 \pm 7)\%$ of the total nucleon spin. Experiments performed at the European Organization for Nuclear Research (CERN) by the European Muon Collaboration (EMC) found out that only $(21.06 \pm 7)\%$ of the nucleon spin is carried by the quarks [1] [2]. Other experiments at CERN (spin muon collaboration (SMC)) and SLAC (E142 and E143) did not agree with the naive Quark Parton Model [3]. This reduction is assumed to be caused by a negatively polarized quark sea at low momentum fraction x, which is not considered in quark models. The complete picture of the nucleon spin can be obtained by taking into account the spin contributions from the gluons and sea quarks and in addition to the quark orbital momentum. So the spin of the nucleon can be written as the sum of the following terms [4]:

$$\frac{1}{2} = \frac{1}{2}\Delta\Sigma + \Delta G + L_z,$$

(1.1)

where $\Delta\Sigma = \Delta u + \Delta d + \Delta s$ is the spin contribution from the quarks, ΔG from the gluons and L_z is the orbital angular momentum contribution from the partons (quarks). The spin contribution from each type of quark to the total

1

nucleon spin is from ref[3]:

$$\Delta u = 0.83 \pm 0.03 \tag{1.2}$$

$$\Delta d = -0.43 \pm 0.03 \tag{1.3}$$

$$\Delta s = 0.10 \pm 0.03. \tag{1.4}$$

1.1 The Standard Model

Matter is composed of two types of elementary particles, quarks and leptons, which form composite particles by exchanging bosons, yet another type of elementary particle. The Standard Model of particle physics, a Quantum Field Theory, was developed between 1970 and 1973. The Standard Model describes all of the known elementary particle interactions except gravity. It is the collection of the following related theories: quantum electrodynamics, the Glashow-Weinberg-Salam theory of electroweak processes, and quantum chromodynamics.

The Standard Model describes a nucleon, a neutron or proton, as a particle composed of three constituent quarks. Quarks are spin 1/2 particles with fractional charge (e_q) and come in the flavors of strange (s), charm (c), beauty (b) and top (t) in addition to up (u) and down (d). Quarks have Baryon quantum number (B') of 1/3. The quantum numbers of quarks with their antiparticles are given in Table 1.1.

Quark	Spin	e_q	I_3	B'	C	S	T	B	Antiquark
u(up)	1/2	+2/3	+1/2	+1/3	0	0	0	0	$\bar{u}$
d(down)	1/2	-1/3	-1/2	+1/3	0	0	0	0	$\bar{d}$
c(charm)	1/2	+2/3	0	+1/3	+1	0	0	0	$\bar{c}$
s(strange)	1/2	-1/3	0	+1/3	0	-1	0	0	$\bar{s}$
t(top)	1/2	+2/3	0	+1/3	0	0	+1	0	$\bar{t}$
b(bottom)	1/2	-1/3	0	+1/3	0	0	0	-1	$\bar{b}$

Table 1.1: Quarks in the Quark Model with their quantum numbers and electric charge in units of electron.

1.2 The Quark Parton Model

In 1964 Gell-Mann and Zweig suggested that a proton was composed of pointlike particles in an effort to explain the resonance spectra observed by experiments performed in the 1950's [5]. These pointlike particles, referred to as partons and later quarks, have not been observed as free particles and are considered to be the building blocks of baryons and mesons. The model assumes that partons are identified according to a quantum number called flavor. For example: up (u), down (d) and strange (s) and their antiparticles. This set of flavor quantum numbers can be used within the context of group theory's SU(3) representation to construct isospin wave functions for the nucleon [6].

The constituent quark model describes a nucleon as a combination of three quarks. According to the quark model, two of the three quarks in a proton are labeled as having a flavor "up" and the remaining quark a flavor "down". The two up quarks have fractional charge $+\frac{2}{3}e$ while the down quark has a charge $-\frac{1}{3}e$. All quarks are spin $\frac{1}{2}$ particles. In the quark model, each quark carries one third of the nucleon mass. Since the late 1960's, inelastic scattering experiments have been used to probe a nucleon's excited states. The experiments suggested

that the charge of the nucleon is distributed among pointlike constituents of the nucleon. The experiments at the Stanford Linear Accelerator Center (SLAC) used high 19.5 GeV energy electrons Coulomb scattered by nucleons through the exchange of a virtual photon [7]. The spacial resolution (d) available using the electron probe may be written in terms of the exchanged virtual photon's four-momentum, Q, such that the electron probe's ability to resolve the contituents of a proton increases as the four momentuum Q increased according to

$$d = \frac{\hbar c}{Q} = \frac{0.2 \text{ GeV} \cdot \text{ fm}}{Q}, \qquad (1.5)$$

and

$$Q^2 = 4EE' \sin^2 \frac{\theta}{2}, \qquad (1.6)$$

where E and E' are the initial and final energy of the lepton and θ is the polar angle of the scattered electron.

The electron scattering data taken during the SLAC experiments revealed a scaling behavior, which was later referred to as Bjorken scaling. The inelastic cross section was anticipated to fall sharply with Q^2 like the elastic cross section. However, the observed limited dependence on Q^2 suggested that the nucleons constituents are pointlike dimensionless scattering centers.

Independently, Richard Feynman introduced the Quark Parton Model, where the nucleons are constructed from three pointlike constituents, called partons. Shortly afterwards, it was discovered that partons and quarks are the same particles. In the QPM, the mass of the quark is much smaller than in the naive Quark Model. In the parton model, the inelastic electron nucleon interaction via a virtual photon is understood as an incoherent elastic scattering processes

between the electron and the constituents of the target nucleon. In other words, a single interaction does not happen with the nucleon as a whole, but with exactly one of its constituents [7]. In addition, two categories of quarks were introduced, "sea" and "valence" quarks. The macroscopic properties of the particle are determined by its valence quarks. On the other hand, the so called sea quarks, virtual quarks and antiquarks, are constantly emitted and absorbed by the vacuum.

The Quark Parton Model predictions are in agreement with the experimental results. One of those predictions is the magnetic moment of baryons. For example, the magnetic moment of the proton should be the sum of the magnetic moments of the constituent quarks according to the naive Quark Model [9] :

$$\frac{e}{2m_p}\mu_p = \Sigma_{i=1,2,3} < P_{\frac{1}{2}}|\frac{e_q(i)\sigma_z(i)}{2m_p(i)}|P_{\frac{1}{2}} > .\qquad(1.7)$$

Assuming that the masses of light non-strange quarks are just one third of the total nucleon mass $m_d = m_u = \frac{m_p}{3} = \frac{m_n}{3}$ and expressing the magnetic moment in units of $\frac{e}{2m_p}$ we get the following result for the proton magnetic moment $\mu_p = 3$, which agrees with experimental findings. The Quark Parton Model predictions of magnetic moments of the other baryons are compared with the experimental results below in Table 1.2. As it can be observed, it is in agreement with experiment within an accuracy of $20 - 25\%$.

The Quark Parton Model has successfully explained the baryon mass spectrum. The baryon masses can be expressed in the quark model using the de Rujula-

Particle	The Quark Model Prediction	Experimental Result
p	3	2.79
n	-2	-1.91
Λ	-0.5	-0.61
Σ^+	2.84	2.46
Σ^-	-1.16	-1.16 ± 0.03
Ξ^0	-1.33	-1.25 ± 0.01
Ξ^-	-0.33	-0.65 ± 0.04

Table 1.2: Magnetic moment of baryons in units of nuclear magnetons $\left(\frac{e}{2m_p}\right)$ [9].

Georgi-Glashow approach:

$$m_B = \Sigma_i m_q(i) + b\Sigma_{i \neq j} \frac{\sigma(i)\sigma(j)}{m_q(i)m_q(j)}. \tag{1.8}$$

The difference between the actual experimental results and the predictions is on the order of 5 - 6 MeV. However, a similar formula for meson masses fails. The difference between the experiment and calculation in the meson case is approximately 100 MeV. This can be explained by calculating the average mass of the quark in a baryon and meson (Table 1.3) [9] :

$$< m_q >_M = \frac{1}{2}(\frac{1}{4}m_\pi + \frac{3}{4}m_p) = 303 \text{MeV} \tag{1.9}$$

$$< m_q >_B = \frac{1}{3}(\frac{1}{2}m_N + \frac{1}{2}m_\Delta) = 363 \text{MeV}. \tag{1.10}$$

Particle	Prediction (MeV/c^2)	Experiment (MeV/c^2)
N	930	940 ± 2
Δ	1230	1232 ± 2
Σ	1178	1193 ± 5
Λ	1110	1116 ± 1
Σ*	1377	1385 ± 4
Ξ	1329	1318 ± 4
Ξ*	1529	1533 ± 4
Ω	1675	1672 ±1

Table 1.3: Baryon mass predictions compared with experimental findings [9] [10].

1.3 Lattice QCD

Although the naive Quark Model successfully described several nucleon properties, it was not a fundamental theory, opening the doorway for the development of new field theory called Quantum Chromodynamics. In the Quark Model, the particles of the baryon decuplet are symmetric in spin and flavor, so that the wave functions that describe the fermions are fully symmetric and identical, which is a violation of the Pauli principle. As a solution, Quantum Chromodynamics suggested that quarks carry an additional degree of freedom, "color". Quarks have three degrees of freedom: spin, flavor and color. There are three states of color: red, green and blue. The Quark Model has color.

Deep inelastic lepton nucleon scattering experiments give us an opportunity to measure the momentum weighted probability density function of partons in the proton and neutron. The fraction of the nucleon momentum carried by quarks can be calculated by integrating the probability density function (F_2):

$$\frac{18}{5}\int_0^1 dx F_2^{eN}(x) = \int_0^1 dx[u(x) + d(x) + \overline{d}(x) + \overline{u}(x)]. \qquad (1.11)$$

The last expression shows that the quarks inside the nucleon carry about 50% of the total four momentum. It leads to the question, are quarks the only particles inside the nucleon? In addition to quarks and antiquarks, there are other components in the nucleon. They can not be seen by using an electromagnetic (electron) nor a weak (neutrino) probe, because they do not carry weak or electric charge.

The scaling behavior was explained by the assumption that a nucleon is built from non-interacting pointlike quarks and antiquarks. However, the quarks were found to be charged particles, which implies that there should be at least an electromagnetic interaction between the nucleon constituents. The spacial and temporal resolution of the target nucleon's probe can be increased with high four-momentum transferred squared Q^2. Using high Q^2, quarks that are seen as pointlike particles at low Q^2 will be resolved into more partons in the nucleon. One can see that inside the nucleon there are more components then just three charged quarks. Due to the scaling violation, the total four momentum of the nucleon is divided over more partons, and the average fractional momentum of each parton will decrease as indicated in Figure 1.1.

It was concluded that a nucleon consists of three main quarks called "valence" quarks, which carry the quantum numbers of the nucleon as well as a "sea" of quark-antiquark pairs. The interaction between the quark-antiquark pairs is mediated by gluons. Unlike QED, where the force mediator (photon) doesn't carry the charge, in QCD, the gluon has a color charge and can interact with other gluons. In other words, QCD is a theory where a field quanta is at the same time a field source. That makes QCD a non-Abelian field theory. QCD
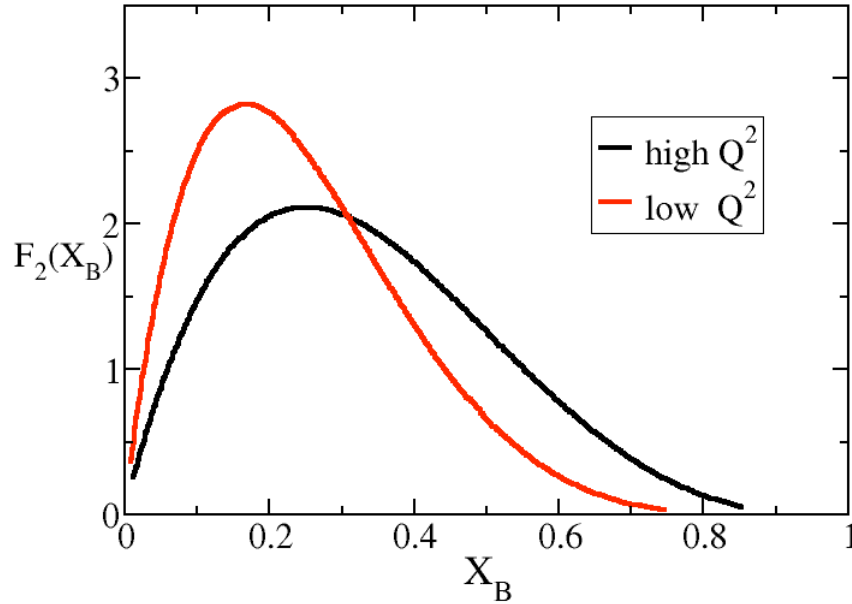
Fig. 1.1: Scaling violation [7].

allows the following interactions:

$$q \rightarrow q + g, \tag{1.12}$$

$$g \rightarrow q + \bar{q}, \tag{1.13}$$

and

$$g \rightarrow g + g. \tag{1.14}$$

The colors carried by the eight gluons are the following: $R\bar{B}$, $R\bar{G}$, $B\bar{R}$, $G\bar{R}$, $B\bar{G}$, $G\bar{B}$, $(R\bar{R}-G\bar{G})/\sqrt{2}$, $(R\bar{R}+G\bar{G}-2B\bar{B})/\sqrt{6}$. The color is not experimentally observable, only "colorless" quark-antiquark systems are observed: baryons

9

(qqq), mesons ($q\bar{q}$) and antibaryons ($\bar{q}\bar{q}\bar{q}$).

The confinement of the quark antiquark system can be explained by the fact that the color force increases when the particle separation increases. As separation decreases the force decreases so that the quarks no longer interact. This phenomenon is referred as an asymptotic freedom. The strong coupling in QCD is defined to first order as follows [7]:

$$\alpha_s(Q^2) = \frac{1}{\beta_0 ln(Q^2/\Lambda_{QCD}^2)} \tag{1.15}$$

$$\beta_0 = \frac{33 - 2n_f}{12\pi}. \tag{1.16}$$

Λ_{QCD} is found experimentally and n_f is the number of active quark flavors. At $Q^2 \sim \Lambda_{QCD} \sim 200$ MeV, $\alpha_s \to \infty$ quark confinement takes place. Perturbative QCD is used to describe deep inelastic scattering, because of its capacity to calculate more than a few non-perturbative quantities within QCD. The two most important aspects of QCD are confinement and asymptotic freedom. Since QCD is a quantum field theory, confinement and asymptotic freedom are related to the running of the coupling constant.

- Confinement states that as the distance between two color charges increases, or the four momentum transferred squared goes to zero, the coupling constant increases. When two color charge constituents move apart, the interaction between them increases so that color-anticolor pairs are created from the vacuum. Hadronization describes the process of recombination of the initial color charges to form a colorless object.

- As the distance between quarks goes to zero the interaction between them

goes to zero asymptoticaly. Due to this property, quarks in the nucleon are free particles. The asymptotic freedom is the cause of the falling of the coupling constant as the distance between charges decreases, or the four momentum transferred square goes to infinity.

1.4   Semi-Inclusive Deep Inelastic Scattering

Deep inelastic scattering (DIS) of leptons by nucleons is a powerful experimental tool for investigating the structure of nucleons. In these experiments, both charged (electrons, muons) and neutral (neutrinos) leptons are used with their antiparticles. In deep inelastic scattering, the scattering occurs on a single nucleon or on bound protons and neutrons inside the nucleus. At large momentum transfer the inelastic scattering is the incoherent sum of elastic scattering off the nucleon constituents, which are assumed to be dimensionless pointlike quarks. In the Constituent Quark Model (CQM) the constituents of the hadron are up and down quarks, whereas in Quantum Chromodynamics the nucleon is a composition of quarks, antiquarks and gluons. In inclusive deep inelastic scattering (IDIS), only the lepton is detected in the final state, whereas in the case of semi-inclusive deep inelatic scattering (SIDIS), a hadron is detected in coincidence with the scattered lepton. Both physics processes can be characterized by a differential cross section. The cross section is proportional to the event rate. The differential cross section for inclusive deep inelastic scattering can be written in terms of a lepton and a hadronic tensor [8] :

$$\frac{d^2\sigma}{dxdQ^2} \propto L_{\mu\nu}W^{\mu\nu}, \tag{1.17}$$

where

$$L_{\mu\nu}(k, k') = 2(k_\mu k'_\nu + k'_\mu k_\nu - \frac{1}{2}Q^2 g_{\mu\nu}), \qquad (1.18)$$

and

$$W^{\mu\nu} = -W_1 \left(g_{\nu\mu} + \frac{1}{Q^2}q_\mu q_\nu \right) + \frac{1}{M^2}W_2 \left(p_\mu + \frac{p \cdot q}{Q^2}q_\mu \right) \left(p_\nu + \frac{p \cdot q}{Q^2}q_\nu \right). \quad (1.19)$$

The leptonic tensor $L_{\mu\nu}$ describes the coupling between the scattering lepton and the virtual photon. The hadronic tensor $W^{\mu\nu}$ describes the absorption of the virtual photon by the target nucleon. The hadronic tensor contains information about the nucleon structure. It can be written in terms of structure functions using symmetry arguments and conservation laws. However, the information about the spin distribution inside the nucleon is contained in the asymmetric part of the hadronic tensor, which can be obtained by taking the difference of the cross sections with opposite spin states of the initial lepton. Polarized quark distribution functions can be extracted from SIDIS measurements using the quark flavor tagging method and exclude the quark flavor assumptions used in inclusive DIS measurements. In SIDIS, the double spin asymmetry can be expressed in terms of the cross sections of final state hadrons produced in the experiment [11]:

$$A_1^h = \frac{\sigma_{1/2}^h - \sigma_{3/2}^h}{\sigma_{1/2}^h + \sigma_{3/2}^h}, \qquad (1.20)$$

where $\sigma_{1/2}^h(\sigma_{3/2}^h)$ represents the semi-inclusive cross section of type h hadrons

produced in the final state when the spin of the initial lepton beam is antiparallel (parallel) to the target nucleon spin.

The semi-inclusive cross section can be expressed in terms of quark distribution functions and fragmentation functions:

$$\frac{d^3\sigma^h_{1/2(3/2)}}{dxdQ^2dz} \approx \Sigma_q e_q^2 q^{+(-)}(x, Q^2) D_q^h(z, Q^2), \tag{1.21}$$

where $q^{+(-)}(x, Q^2)$ is the quark distribution function with spin oriented parallel (antiparallel) to the spin of the nucleon and the fragmentation function $D_q^h(z, Q^2)$ is a measure of the probability that a quark of flavor q will fragment into a hadron of type h.

The measured structure function in inclusive deep inelastic scattering experiments contains the contribution from all the different quark flavors to the total nucleon momentum and spin, without distinguishing the contribution from the individual quark flavors. On the other hand, semi-inclusive deep inelastic scattering experiments provide an opportunity to determine the struck quark flavor by detecting the final state hadron in coincidence with the scattered lepton. The kinematics of single pion electroproduction in SIDIS can be described by five variables: the virtual photon four-momentum transferred squared Q^2, invariant mass of the photon-nucleon system W, the polar $\theta_\pi{}^*$ and the azimuthal angle $\varphi_\pi{}^*$ of the outgoing pion in the center of mass frame, and the scattered electron azimuthal angle φ_e.

The incoming electron with four momentum $k = (E, \vec{k})$ is scattered from the target of four momentum $(M, \vec{0})$, where M represents the rest mass of the
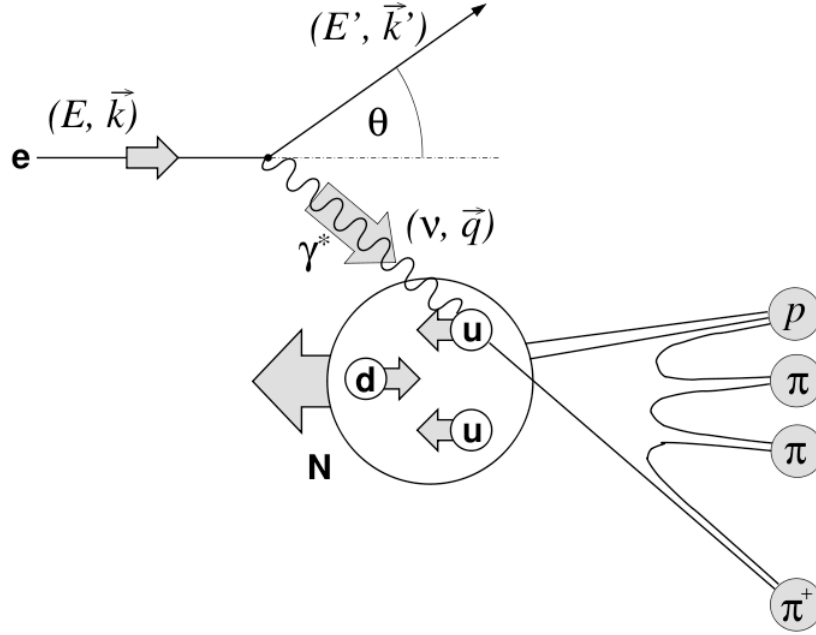
Fig. 1.2: Diagram of the Semi-Inclusive Deep Inelastic Scattering [11].

target nucleon. The four momentum of the scattered electron and hadron are respectively $k' = (E', \vec{k'})$ and $p_h = (E_h, \vec{p_h})$. Semi-inclusive deep inelastic scattering is depicted in Figure 1.2. The four momentum of the exchanged virtual photon, through which the SIDIS occurs, is the four momentum lost by the initial electron $q = k - k'$. The negative square of the four momenta can be written as $Q^2 = -q^2|_{lab} = 4EE' \sin^2 \frac{\theta}{2}$, where Q^2 is greater then zero. The energy transferred from the scattered electron to the target nucleon, which is also the energy of the virtual photon, is given by

$$\nu = \frac{p \cdot q}{M} = E - E'|_{lab}. \tag{1.22}$$

14

The Bjorken scaling variable x is defined as

$$x = \frac{Q^2}{2p \cdot q} = \frac{Q^2}{2M\nu}.$$ (1.23)

The fraction of the virtual photon energy transferred to a hadron, that is detected in the final state in coincidence with the scattered electron, is

$$z = \frac{p \cdot p_h}{p \cdot q} = \frac{E_h}{\nu}|_{lab},$$ (1.24)

where the last kinematic variable is the invariant mass of the scattering process available to produce the final hadronic state

$$W^2 = (q + p_h)^2 = M^2 + 2M\nu - Q^2.$$ (1.25)

The electron scattering cross section off a nucleon can be written as [8] :

$$\frac{d^2\sigma}{dQ^2dW^2} = \frac{2\pi\alpha^2 M}{(s - M^2)^2 Q^2}\left[2W_1(W^2, Q^2) + W_2(W^2, Q^2)\left(\frac{(s - M^2)(s - W^2 - Q^2)}{M^2 Q^2} - 1\right)\right],$$ (1.26)

where s is $(p + k)^2$. In the target rest frame it can be expressed in terms of the initial and final energies of the electron and the electron scattering angle θ:

$$\frac{d^2\sigma}{d\Omega dE'} = \frac{\alpha^2 M}{8E^2 E_p \sin^4\frac{\theta}{2}}\left[2W_1 \sin^2\frac{\theta}{2} + W_2\frac{4E_p^2}{M^2}\cos^2\frac{\theta}{2}\right],$$ (1.27)

15

$k = (E, \vec{k}), \, k = (E^{'}, k^{'})$	4 - momenta of the initial and final state leptons
$\theta, \, \phi$	Polar and azimuthal angle of the scattered lepton
$P^{lab} = (M, \vec{0})$	4 - momentum of the initial target nucleon
$q = k - k^{'}$	4 - momentum of the virtual photon
$Q^2 = -q^{2lab} = 4EE^{'} \sin^2 \frac{\theta}{2}$	Negative squared 4 - momentum transfer
$\nu = \frac{Pq}{M} = E - E^{'}|^{lab}$	Energy of the virtual photon
$x = \frac{Q^2}{2Pq} = \frac{Q^2}{2M\nu}$	Bjorken scaling variable
$y = \frac{Pq}{Pk} = \frac{\nu}{E}|_{lab}$	Fractional energy of the virtual photon
$W^2 = (P + q)^2 = M^2 + 2M\nu - Q^2$	Squared invariant mass of the photon-nucleon system
$p_h = (E_h, \vec{p_h})$	4 - momentum of a hadron in the final state
$z = \frac{P \cdot p_h}{P \cdot q} = \frac{E_h}{\nu}|_{lab}$	Fractional energy of the observed final state hadron

Table 1.4: Kinematic variables in deep inelastic scattering.

where W_1 and W_2 are so called structure functions, E_p and E the energy of the initial proton and electron respectively and θ the polar angle of the scattered electron. M is the mass of the target, in our case the nucleon.

As mentioned above, the DIS interaction does not happen with the hadron as a whole, but with one of its constituents. Each quark (constituent) carries the fraction four-momentum x of the nucleon with probability density $q(x)$. $q(x)$ is the probability of finding the qth quark with fraction x of the nucleon four-momentum. Under these assumptions, the structure functions can be written as a sum of the elastic structure functions weighted by $q(x)$. Taking into consideration that the mass of the ith quark is also the fraction x of the nucleon

mass $M_q = xM_h$:

$$W_1(Q^2, \nu) = \Sigma_q \int_0^1 dx q(x) e_q^2 \frac{Q^2}{4x^2 M_h^2} \delta\left(\nu - \frac{Q^2}{2M_h x}\right) = \Sigma_q e_q^2 q(x_B) \frac{1}{2M_h}, \quad (1.28)$$

and

$$W_2(Q^2, \nu) = \Sigma_q \int_0^1 dx q(x) e_q^2 \delta\left(\nu - \frac{Q^2}{2M_h x}\right) = \Sigma_q e_q^2 q(x_B) \frac{x_B}{\nu}. \quad (1.29)$$

It was experimentally shown that the measured cross section of inelastic lepton-nucleon scattering depends only on x_B. As was mentioned this referred to as scaling. If there where additional objects inside the nucleon besides the main building partons, it would introduce new energy scales. The experimental observation of the scaling phenomenon was the first evidence that quarks are the constituents of the hadron. The results which were obtained from the MIT-SLAC Collaboration (1970) are presented below on Figure 1.3 and Figure 1.4 [7] [8]. It clearly shows the structure function W_2's dependence on x_B and independence of the four-momentum transfer squared.

The DIS of the unpolarized electron by a nucleon can be described in terms of two structure functions, $F_1(x)$ and $F_2(x)$

$$F_1(x) = M_h W_1 = \frac{1}{2} \Sigma_q e_q^2 q(x), \quad (1.30)$$

and

$$F_2(x) = \nu W_2 = \frac{1}{2} \Sigma_q x e_q^2 q(x). \quad (1.31)$$
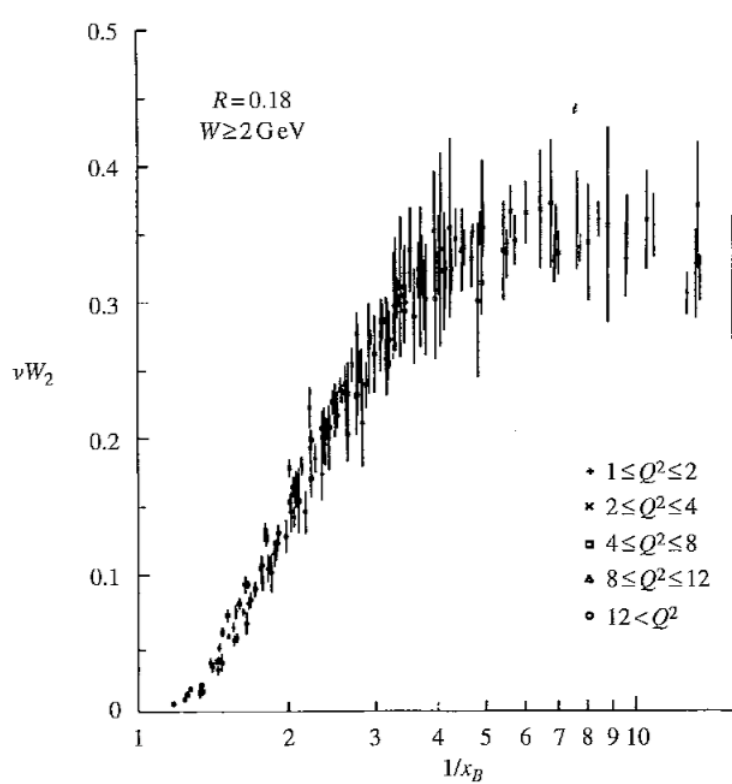
Fig. 1.3: Scaling behavior of $\nu W_2(1/x_B) = F_2(1/x_B)$ for various Q^2 ranges [7].

The structure function F_1 measures the parton density, while F_2 describes the momentum density. The relation between the structure functions $F_1(x)$ and $F_2(x)$ is given by the following equation:

$$F_2(x)\frac{1+\gamma^2}{1+R} = 2xF_1(x), \tag{1.32}$$

where $R(x, Q^2)$ is the ratio of longitudinal to transverse deep inelastic scattering cross sections and $\gamma = \sqrt{\frac{Q^2}{\nu^2}}$. In the naive Quark Parton Model, the longitudinal-transverse interference is neglected. In the Bjorken limit it can be
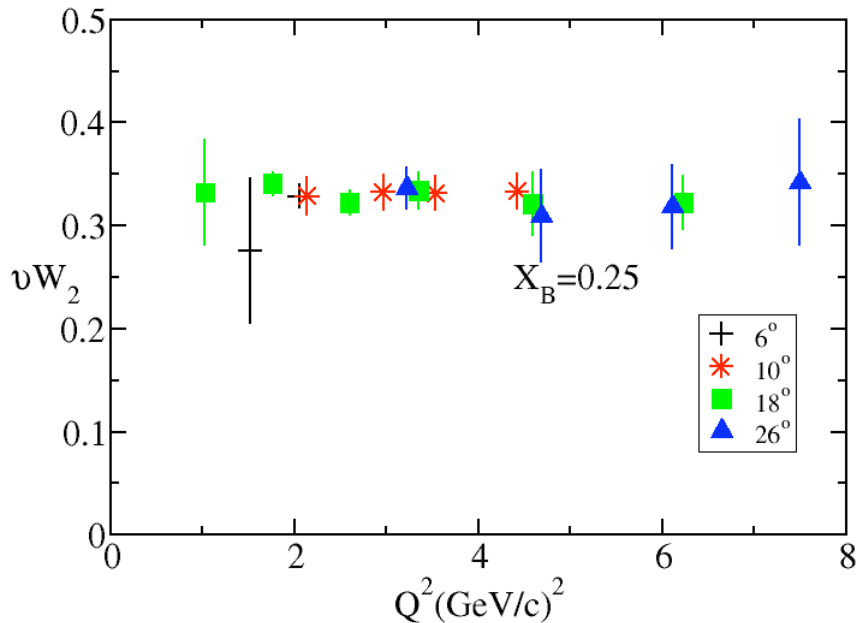
Fig. 1.4: Value of $\nu W_2(Q^2) = F_2(Q^2)$ for $x_B = 0.25$ [7].

reduced to the Callan-Gross relation:

$$F_2(x) = 2xF_1(x). \tag{1.33}$$

The distributions of up and down quarks in the nucleon are defined as $u(x)$ and $d(x)$. There are two categories of quarks: valence and sea quarks $u(x) = u_v(x) + u_s(x)$, assuming that $u_s(x) = \bar{u}(x)$. The constituent quark model (CQM or QPM) states that the proton (neutron) contains two up (down) quarks and one down (up) quark. Summing over all the constituents of a proton should

result in the following sum rule:

$$\int_0^1 dx u_v(x) = 2, \tag{1.34}$$

and

$$\int_0^1 dx d_v(x) = 1. \tag{1.35}$$

The electromagnetic structure function for the proton and neutron can be expressed in terms of the quark distribution functions:

$$F_2^{ep} = \frac{4}{9} \left[xu(x) + x\bar{u}(x) + xc(x) + x\bar{c}(x) \right] + \frac{1}{9} \left[xd(x) + x\bar{d}(x) + xs(x) + x\bar{s}(x) \right]. \tag{1.36}$$

F_2^{en} can be obtained from F_2^{ep} by replacing $u \to d$ and vice versa.

From the last two equations, the structure functions for the proton and neutron can be written in terms of the valence quark distribution functions:

$$F_2^{ep} = x \left[\frac{4}{9} u_v(x) + \frac{1}{9} d_v(x) \right], \tag{1.37}$$

and

$$F_2^{en} = x \left[\frac{4}{9} d_v(x) + \frac{1}{9} u_v(x) \right]. \tag{1.38}$$

For most fixed-target experiments like CLAS run group EG1b (EG1b), the spin asymmetry is given by the ratio of the polarized structure function to the unpolarized:

$$A(x, Q^2) = \frac{g_1(x)}{F_1(x)}, \tag{1.39}$$

where the polarized structure function $g_1(x)$ represents the helicity difference of quark number densities. The spin asymmetry A and the unpolarized structure function F_1 are measurable quantities and through them one can determine $g_1(x)$, which maybe expressed as:

$$g_1(x) = \frac{1}{2}\Sigma_q e_q^2 (q^+(x) - q^-(x)) \equiv \frac{1}{2}\Sigma_q e_q^2 \Delta q(x), \qquad (1.40)$$

where $q^{+(-)}(x)$ is the quark distribution function with spin oriented parallel (antiparallel) to the spin of the nucleon.

1.4.1 Fragmentation Independent

The asymmetries from semi-inclusive pion electroproduction using proton or deuteron targets can be written in terms of the difference of the yield from oppositely charged pions [12]:

$$A_{1,p}^{\pi^+ \pm \pi^-} = \frac{\Delta\sigma_p^{\pi^+ \pm \pi^-}}{\sigma_p^{\pi^+ \pm \pi^-}} = \frac{[(\sigma_p^{\pi^+})_{1/2} - (\sigma_p^{\pi^+})_{3/2}] \pm [(\sigma_p^{\pi^-})_{1/2} - (\sigma_p^{\pi^-})_{3/2}]}{[(\sigma_p^{\pi^+})_{1/2} + (\sigma_p^{\pi^+})_{3/2}] \pm [(\sigma_p^{\pi^-})_{1/2} + (\sigma_p^{\pi^-})_{3/2}]},$$
$$(1.41)$$

$$A_{1,2H}^{\pi^+ \pm \pi^-} = \frac{\Delta\sigma_{2H}^{\pi^+ \pm \pi^-}}{\sigma_{2H}^{\pi^+ \pm \pi^-}} = \frac{[(\sigma_{2H}^{\pi^+})_{1/2} - (\sigma_{2H}^{\pi^+})_{3/2}] \pm [(\sigma_{2H}^{\pi^-})_{1/2} - (\sigma_{2H}^{\pi^-})_{3/2}]}{[(\sigma_{2H}^{\pi^+})_{1/2} + (\sigma_{2H}^{\pi^+})_{3/2}] \pm [(\sigma_{2H}^{\pi^-})_{1/2} + (\sigma_{2H}^{\pi^-})_{3/2}]}.$$
$$(1.42)$$

Independent fragmentation identifies the process in which quarks fragment into hadrons, independent of the photon-quark scattering process. In other words, the fragmentation process is independent of the initial quark environment, which initiates the hadronization process. Assuming independent fragmentation and using isospin ($D_u^{\pi^+} = D_{\bar{u}}^{\pi^-}$ and $D_d^{\pi^-} = D_{\bar{d}}^{\pi^+}$) and charge ($D_u^{\pi^+} = D_d^{\pi^-}$)

conjugation invariance for the fragmentation functions, the following equality holds:

$$D_u^{\pi^+ \pm \pi^-} = D_u^{\pi^+} \pm D_u^{\pi^-} = D_d^{\pi^+ \pm \pi^-}. \tag{1.43}$$

The polarized and unpolarized cross sections for pion electroproduction can be written in terms of valence quark distribution functions in the valence region as:

$$\Delta\sigma_p^{\pi^+ \pm \pi^-} = \frac{1}{9} \left[4(\Delta u + \Delta \bar{u}) \pm (\Delta d + \Delta \bar{d}) \right] D_u^{\pi^+ \pm \pi^-} \tag{1.44}$$

$$\Delta\sigma_n^{\pi^+ \pm \pi^-} = \frac{1}{9} \left[4(\Delta d + \Delta d^-) \pm (\Delta u + \Delta u^-) \right] D_u^{\pi^+ \pm \pi^-} \tag{1.45}$$

$$\Delta\sigma_{2H}^{\pi^+ \pm \pi^-} = \frac{5}{9} \left[(\Delta u + \Delta \bar{u}) \pm (\Delta d + \Delta \bar{d}) \right] D_u^{\pi^+ \pm \pi^-} \tag{1.46}$$

and unpolarized:

$$\sigma_p^{\pi^+ \pm \pi^-} = \frac{1}{9} \left[4(u + \bar{u}) \pm (d + \bar{d}) \right] D_u^{\pi^+ \pm \pi^-} \tag{1.47}$$

$$\sigma_n^{\pi^+ \pm \pi^-} = \frac{1}{9} \left[4(d + \bar{d}) \pm (u + \bar{u}) \right] D_u^{\pi^+ \pm \pi^-} \tag{1.48}$$

$$\sigma_{2H}^{\pi^+ \pm \pi^-} = \frac{5}{9} \left[(u + \bar{u}) \pm (d + \bar{d}) \right] D_u^{\pi^+ \pm \pi^-}. \tag{1.49}$$

In the valence region $(x_B > 0.3)$, where the sea quark contribution is minimized, the above asymmetries can be expressed in terms of polarized and unpolarized valence quark distributions:

$$A_{1,p}^{\pi^+ \pm \pi^-} = \frac{4\Delta u_v(x) \pm \Delta d_v(x)}{4 u_v(x) \pm d_v(x)} \tag{1.50}$$

$$A_{1,2H}^{\pi^+ \pm \pi^-} = \frac{\Delta u_v(x) + \Delta d_v(x)}{u_v(x) + d_v(x)}. \tag{1.51}$$

The ratio of polarized to unpolarized valence up and down quark distributions may then be written as

$$\frac{\Delta u_v}{u_v}(x, Q^2) = \frac{\Delta \sigma_p^{\pi^+ - \pi^-} + \Delta \sigma_{2H}^{\pi^+ - \pi^-}}{\sigma_p^{\pi^+ - \pi^-} + \sigma_{2H}^{\pi^+ - \pi^-}}(x, Q^2), \tag{1.52}$$

and

$$\frac{\Delta d_v}{d_v}(x, Q^2) = \frac{\Delta \sigma_p^{\pi^+ - \pi^-} - 4\Delta \sigma_{2H}^{\pi^+ - \pi^-}}{\sigma_p^{\pi^+ - \pi^-} - 4\sigma_{2H}^{\pi^+ - \pi^-}}(x, Q^2). \tag{1.53}$$

The ratio of polarized to unpolarized valence quark distribution functions can be extracted using the last two equations.

1.4.2 Independent Fragmentation Function Test

A test of independent fragmentation can be performed by probing polarized proton and neutron targets with polarized electrons. The ratio of the difference of polarized to unpolarized cross sections for proton and neutron targets $(\Delta R_{np}^{\pi^+ + \pi^-})$ can be written in terms of the structure functions:

$$
\begin{aligned}
\Delta R_{np}^{\pi^+ + \pi^-} &= \frac{\Delta \sigma_p^{\pi^+ + \pi^-} - \Delta \sigma_n^{\pi^+ + \pi^-}}{\sigma_p^{\pi^+ + \pi^-} - \sigma_n^{\pi^+ + \pi^-}} \\
&= \frac{(\Delta u + \Delta \bar{u}) - (\Delta d + \Delta \bar{d})}{(u + \bar{u}) - (d + \bar{d})}(x, Q^2) \\
&= \frac{g_1^p - g_1^n}{F_1^p - F_1^n}(x, Q^2).
\end{aligned}
\tag{1.54}
$$

The last expression of the asymmetry $\Delta R_{np}^{\pi^+ + \pi^-}$ was obtained from the following

equations:

$$g_1^p - g_1^n = \frac{1}{6} \left[(\Delta u + \Delta \bar{u}) - (\Delta d + \Delta \bar{d}) \right],$$

(1.55)

and

$$F_1^p - F_1^n = \frac{1}{6} \left[(u + \bar{u}) - (d + \bar{d}) \right].$$

(1.56)

Independent fragmentation holds if the ratio of the difference of polarized to unpolarized cross sections for proton and neutron targets $\Delta R_{np}^{\pi^+ + \pi^-}$ depends only on the Bjorken scaling variable (x) and four momentum transferred squared (Q^2) of the quantities g_1 and F_1 measured in deep inelastic scattering, and is independent of the fractional energy of the observed final state hadron (z).

CHAPTER 2

Experimental Setup

2.1 Target

2.1.1 Introduction

Polarized targets and polarized beams were recently acquired research tools used to investigate the spin structure of the nucleon. Inclusive scattering experiments using polarized targets and beams facilitate measurements of observables exhibiting spin degrees of freedom, like the spin structure of the nucleon, the electromagnetic structure of the nucleon in its ground state, etc [13]. The technology for producing targets containing polarized nucleons has been developed over the past 50 years. For experiments using electrons as probes, due to the small cross section of the electromagnetic interactions, one of the requirements for polarized targets are a large thickness and resistance to the radiation damage caused by a high electron beam intensity. The solid NH_3 and ND_3 targets for the EG1b experiment were polarized via the Dynamic Nuclear Polarization (DNP) method [14].

The EG1b polarized target system presented in Figure 2.1 consists of the following main components: superconducting Helmholtz coils capable of producing a 5 T magnetic field, an evaporation refrigerator for target cooling to LHe tem-

peratures, microwaves to induce spin flip in the target, an NMR system to measure the target polarization, and housing for the solid target [13].
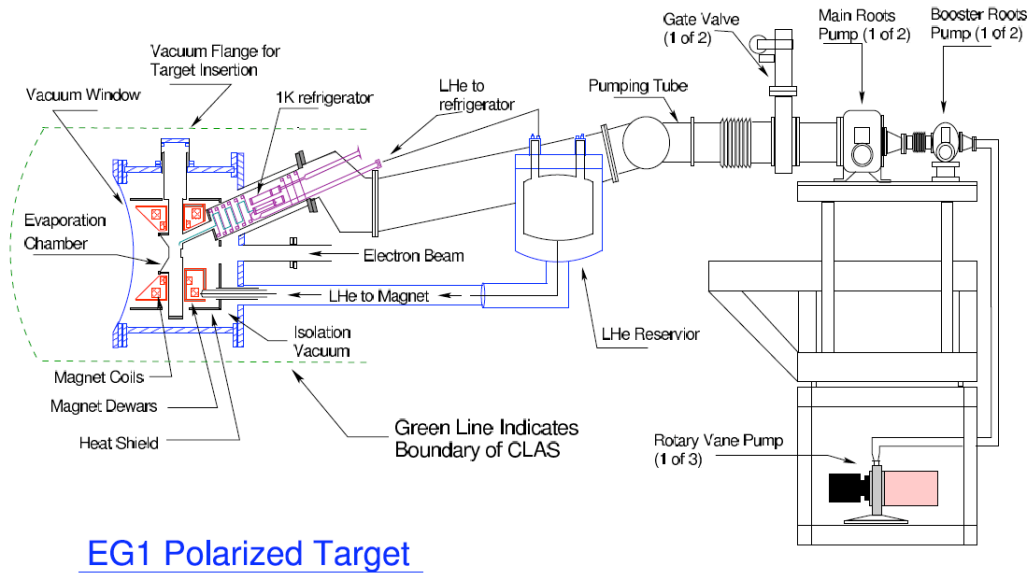
Fig. 2.1: EG1b Polarized Target System.

Target Magnet

A 5 T magnetic field is established using a pair of superconducting Helmholtz coils made out of a Niobium-Titanium mixture with a critical temperature of 9 K. The magnet becomes superconducting below its critical temperature. In order to establish a current in the coils, a section of the magnet is warmed above its critical temperature. This process is called "magnet energization". After the coils have been energized, the "magnet switch" section of the coils is cooled down and the current in the leads is ramped down. The full current of the magnet is carried by the superconducting Helmholtz coils (Figure 2.2).

The superconducting coils are oriented such that the magnetic field is parallel to the incident beam direction. The field induces the hyperfine splittings needed

26
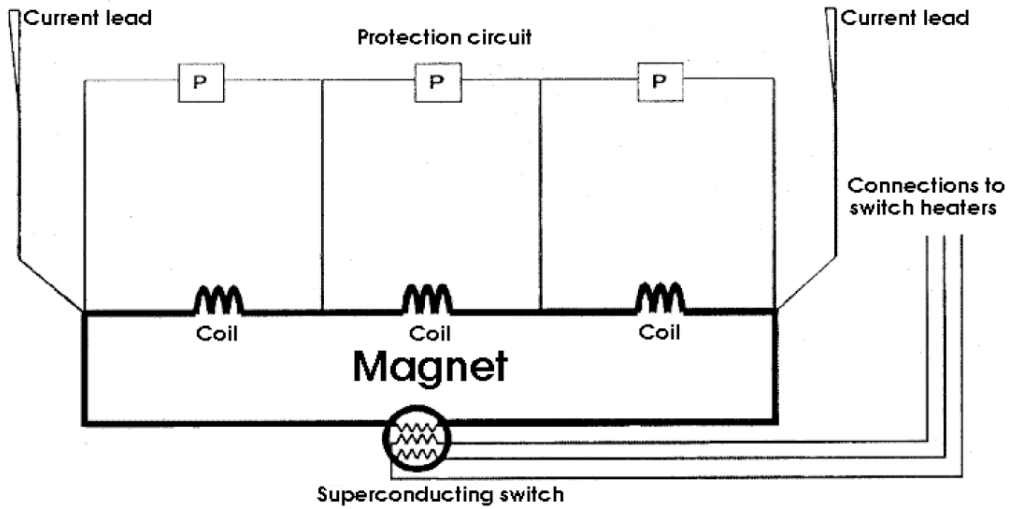
Fig. 2.2: The Schematic of the Target Magnet.

to polarize the target material using a 140 GHz RF wave. The field varies less than 10^{-4} over a cylindrical volume of 20 mm diameter and the target length. This configuration is necessary for DNP. The particles with scattering angles between 0 - 50 degrees as well as 75 - 105 degrees are detected in the CLAS. The Helmholtz coils block particles scattering between 50 and 75 degrees. The target magnetic field does not interact with the electron beam and it is effective in shielding the drift chambers from low energy Moller electrons. The target field falls rapidly with distance as $\sim 1/r^3$ and bends scattered particles in the azimuthal direction. The effect of the magnetic field on the drift chambers is negligible [15] .

The Evaporation Refrigerator

The target material is located at the center of the magnet in a separate chamber, called the banjo. Cooling the target to approximately 1 K was achieved using a ^{4}He evaporation refrigerator inserted through a 20 cm diameter pumping

27

tube. The pumping tube connects the banjo and the pumping system. The components of the refrigerator are the sintered copper separator pot, two series of heat exchangers, and two lines that supply Helium to the banjo. The phase separator allows the liquid to pass, but blocks the Helium vapor. The Helium vapor is pumped away to cool the radiation baffles. The liquid in the phase separator is directed to one of the two banjo lines. The heat exchangers are remotely controlled by needle valves. The presence of the liquid Helium in the target chamber cools the target material effectively [13] .

The Microwave System

The 140 GHz microwave used for DNP is supplied by the Extended Interaction Oscillator (EIO) tube providing 16 Watts of power at the anode with a ~ 2 GHz bandwidth tube. The frequency can be adjusted by mechanically changing the size of the resonant cavity. Using a (10 kV) power supply, the microwave frequency can be finely tuned over a range of 200 MHz [13]. The negative and positive spin states of the nucleon differ by ~ 400 MHz. Because of that, the target polarization orientation can be changed by varying the microwave frequency. Flipping the target spin using microwaves instead of changing the Helmholtz field direction allows one to investigate target polarization systematic effects.

Microwaves are delivered to the target material using a WR-6 rectangular gold-plated wave guide located outside the cryostat and a 5 mm tube made out of CuNi inside the wave guide system. The CuNi tube and the wave guide are connected by a rectangular-circular adapter. This allows microwaves to travel through the tube and into the rectangular segment of the wave guide supplying

microwaves to the desired target cell during the experiment [16].

The Nuclear Magnetic Resonance System

The polarization of the target material during the experiment was monitored using Nuclear Magnetic Resonance (NMR) techniques. The technique relies on detecting nuclear magnetic spin transitions. The rate of transitions is related to the population difference of the energy levels giving information on the original target polarization. The magnetization of the sample, of volume V, with N spins, each with I spin value is [13]

$$\vec{M} = N_{g\mu_N}IP_I = \Sigma_i^N \frac{\vec{\mu}_i}{V}.$$ (2.1)

When the external magnetic field is placed perpendicularly to a rotating resonance frequency field with amplitude and frequency of $\vec{B}_1$ and ω respectively, nuclear Zeeman transitions are induced in the target material. The rate of these transitions allows a measurement of the target polarization. The current in the coil that surrounds the target generates an oscillating resonance frequency. The absorption or emission of energy by the coil (energy gain or loss in the resonance circuit) indicates the sign of the target polarization. A measurement of the ratio of the strengths of the NMR signal with and without RF applied gives the polarization of the target relative to the calculable thermal equilibrium (TE) polarization [13]. The polarization of protons and deuterons at thermal equilibrium are given as

$$P_{TE}^p = \tanh(\frac{\mu_p B}{k_B T})$$ (2.2)

and

$$P_{TE}^{ND_3} = \frac{4\tanh(\mu_d B/2k_B T)}{(3 + \tanh^2(\mu_d B/2k_B T))}, \quad (2.3)$$

where k_B is the Boltzmann constant, B is external magnetic field, μ_p (μ_d) represents proton (deuteron) magnetic moment, and T is temperature. During the experiment, the target polarization using NMR was measured via Q-meters of the Liverpool-type. It measures the voltage and related power gain or loss in the coil as a function of the input frequency. The Q-meter circuit is powered by a generator which sweeps the RF frequency through the Larmor frequency of the target. The inductance of the coil changes when the target absorbs or emits energy, producing the impedance change of circuit. The impedance change is related to the circuit voltage output. After accounting for the background measurement of the Q-meter for the input frequency and calibrating the system via the Thermal Equilibrium measurements, the target polarization is extracted. The NMR technique was only used to monitor the target polarization during the experiment, a final measurement of the polarization relied on measuring the exclusive (quasi-)elastic scattering asymmetry.

The Target Chamber

The target chamber is placed at the top of the cryostat. The chamber is filled with LHe to keep the target material cool. It contains four target cells that are positioned using an aluminum target ladder structure. The cells are made of plastic material (polychlorotrifluoroethylene (PCTFE)) with a wall thickness of 0.2 mm, in order to minimize the amount of material. The target cells are

1.5 cm in diameter and 1 cm in length. The PCTFE material was chosen for its high resistance to radiation damage and for the absence of hydrogen. The aluminum structure is connected to a brass disk minimizing the heat load due to radiation. In order to reduce the thermal conductivity along the target chamber, a teflon block was placed between the aluminum structure and the brass disk. The disk itself is connected to the top flange by a threaded stainless steel rod. The stainless steel rod is attached to the stepping motor [16].
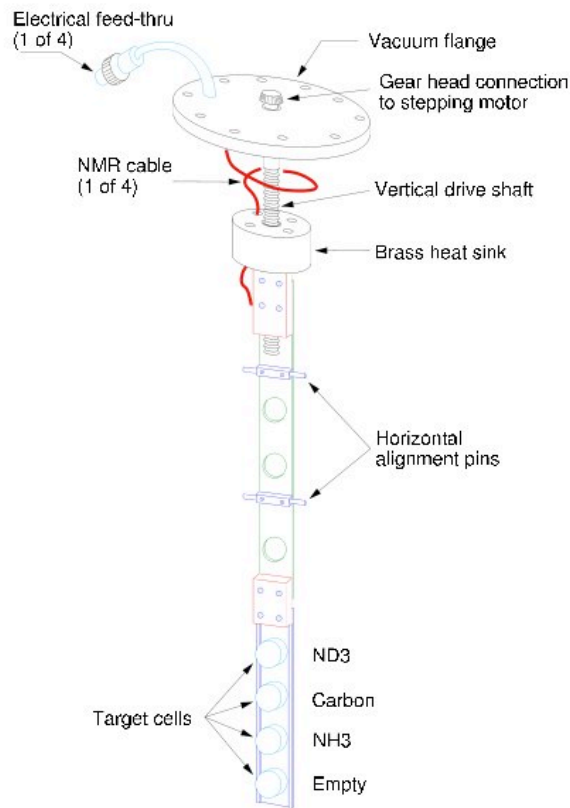
Fig. 2.3: Schematic of the Target Insert.

During the experiment, two of the target cells were filled with NH_3 and ND_3, a third cell with a 2.3 mm thick graphite disk, and the last cell was left empty. The NH_3 and ND_3 targets were used for physics measurements, while the Carbon

and the empty cells for background measurements. The desired target cell can be placed along the beam axis using a stepper motor. The NMR coils were wrapped around the outside surface of the cells. The coils, a 0.15 mm in diameter CuNi tubing, were shaped rectangularly. Only one loop of NMR coils was used for the NH_3 target, while the ND_3 target required four loops to measure the polarization. Temperature sensors were located at several places on the target chamber, and heater coils were attached below each target cell for annealing.

2.1.2 Polarized Target Materials

A polarized solid target's limited resistance to radiation damage is one of the remaining challenges for using polarized targets in scattering experiments. At present, solid ammonia and lithium deuteride are the target materials with the highest resistance to radiation damage [17]. For the EG1b experiment, ammonia targets were selected because of their ability to produce high polarization and be resistant to high radiation dose caused by the incident electron beam. Another advantage of an ammonia target is its high ratio of free nucleons ($\sim 3/18$), approximately 16.7 % for $^{15}NH_3$ and 28.6 % for $^{15}ND_3$. One disadvantage of choosing ammonia is the polarization background caused by ^{15}N (spin - 1/2), or ^{14}N (spin - 1), which was accounted for by taking data using a solid ^{15}N target [18] [15]. The main target materials used for the EG1b experiment were frozen ammonia, $^{15}NH_3$, for the polarized protons and deuterated ammonia, $^{15}ND_3$ for the polarized deuterons. In addition to $^{15}ND_3$ and $^{15}NH_3$ targets, C_{12}, liquid He^4 and solid N_{15} were used to estimate the dilution of the data by

background which can be attributed to the interaction of the incident electron with the Nitrogen or Helium nucleons present in the target cell. This estimate is referred to as a dilution factor [18] .
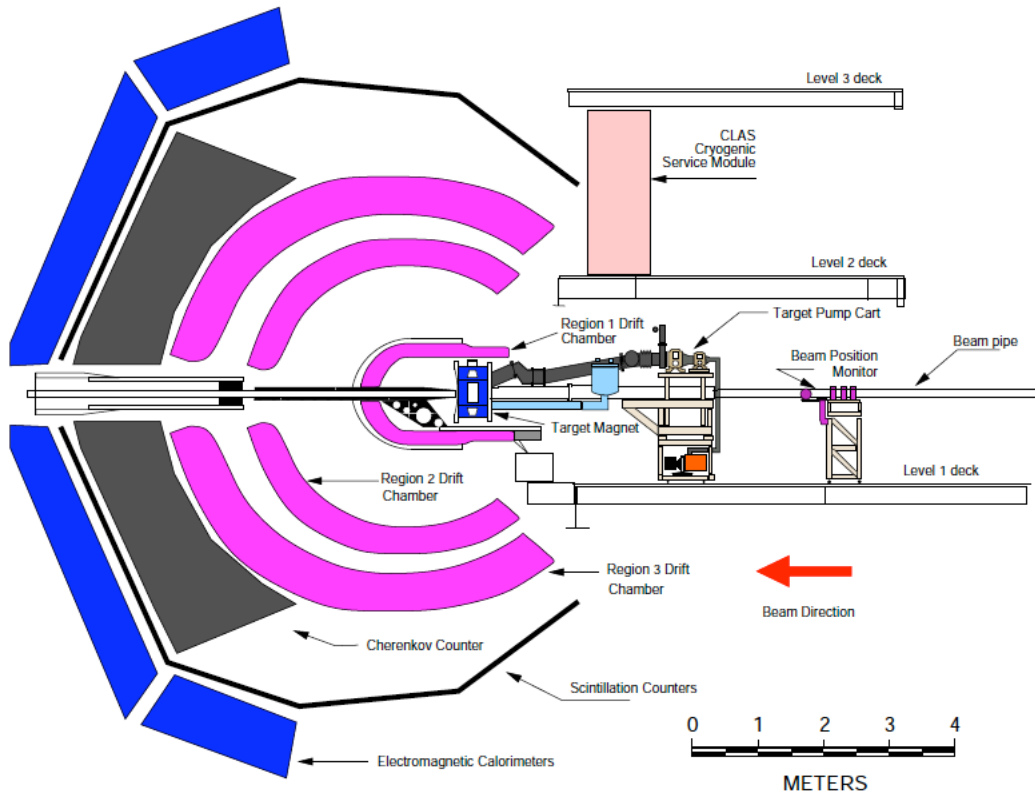
Fig. 2.4: EG1b Polarized Target in The CLAS Detector.

The target materials for the EG1b experiment were prepared by slowly freezing ammonia gas at 77 K and crushing the solid ammonia into small pieces 1 - 3 mm in diameter, at the Polarized Target Lab of the University of Virginia Physics Department. This design of the target helps to cool it effectively using liquid Helium. Free electrons are introduced into the frozen ammonia by irradiating it with an electron beam depositing a dose of 10^{17} electrons/cm^2 at a temperature near 80 K [19]. Dynamic Nuclear Polarization, explained below, uses the free

33

electrons to polarize the nucleii in the target. During the experiment, the polarized target is slowly damaged with the electron beam. This damage can be repaired by warming the target material to 80 K for NH_3, and higher for ND_3. During this annealing, free radicals (paramagnetic centers) produced at low temperatures are recombined, decreasing the number of paramagnetic centers. After repeating this process several times, the target material exhibits significant decrease in the polarization and has to be replaced. The polarized target granules change their color from grey to purple after radiation damage (Figure 2.5).

Fig. 2.5: EG1b target material after the radiation damage.

Dynamic Nuclear Polarization (DNP) is a process in which the polarization of free electrons is transferred to a nucleus [15]. In DNP the target is doped with paramagnetic impurities by chemical doping or by irradiating the target in an electron beam. For low temperatures, on the order of 0.5 K, and high magnetic

fields on the order of 2.5 Tesla, the free electron polarization approaches 100%. The protons inside the target are unpolarized. An applied microwave field with a frequency close to the electron spin resonance induces transitions which flip the spin of the electron and, because of the electron-nucleus hyperfine couping, the spin of the nearby nucleon. The relaxation time of the electron is 10^{-3} s, whereas the relaxation time of the proton in the target is 10^3 s. Due to such a big difference of the relaxation time of the proton and electron, the flipped electron spin rapidly returns to its thermal equilibrium state from where it induces a proton spin-flip again. As a result, the spin polarization is transferred to the protons after some time. The average beam-target polarization product for the EG1b experiment was $P_b \times P_t = (0.51 \pm 0.01)$ and $P_b \times P_t = (0.19 \pm 0.03)$ for the NH_3 and ND_3 targets respectively [20].

2.2 The CEBAF Large Acceptance spectrometer

2.2.1 Introduction

The CEBAF Large Acceptance Spectrometer (CLAS), located in Jefferson Lab's Hall B, was used to measure the final state particles resulting from the scattering of a polarized electron by a polarized nucleon. The CLAS uses six superconducting coils to establish a toroidal magnetic field encircling the incident electron's momentum direction. A set of three drift chambers are positioned to determine the trajectories of particles which pass through the six gaps between the magnet coils. The first drift chamber, Region 1 (R1), is placed at the en-

trance to the magnetic coil. A second chamber, Region 2 (R2), is placed in the center of the coils. The final chamber, Region 3 (R3), measures charged particles leaving the toroidal field. A total of eighteen drift chambers are available to reconstruct the trajectory of charged particles passing through the magnetic field. After the drift chamber system, the CLAS detector is equipped with a Cherenkov counter for separating electrons from pions, and with scintillators, to determine the time of flight of a charged particle. An electromagnetic calorimeter is placed at the exit of the detector to detect neutral particles and improve the detector's ability to distinguish between electrons and hadrons.

2.2.2   The Torus Magnet

The CLAS's torus magnet consists of six superconducting coils located around the beam line in a toroidal geometry, producing a magnetic field in the φ direction when the z-axis of a spherical coordinate system is aligned with the incident beam direction. A sector is defined based on the boundaries of each magnetic coil resulting in a total of six sectors. The maximum current for the CLAS magnet is 2860 Amps corresponding to a total magnetic field in the forward direction of 2.5 T-m and 0.6 T at a polar scattering angle of 90 degrees. The magnet itself is around 5 m in diameter and 5 m in length. The coils of the magnet are cooled by liquid Helium circulating through cooling tubes at the magnet's superconducting temperature of 4.5 K [16]. A charged particle's momentum is determined by the radius of curvature through the magnetic field to a resolution of $\Delta p/p$ from 0.5 % to 1 % [21]. In the EG1b experiment, the operated torus values were: 2250, -2250, 1500, -1500 Amps.
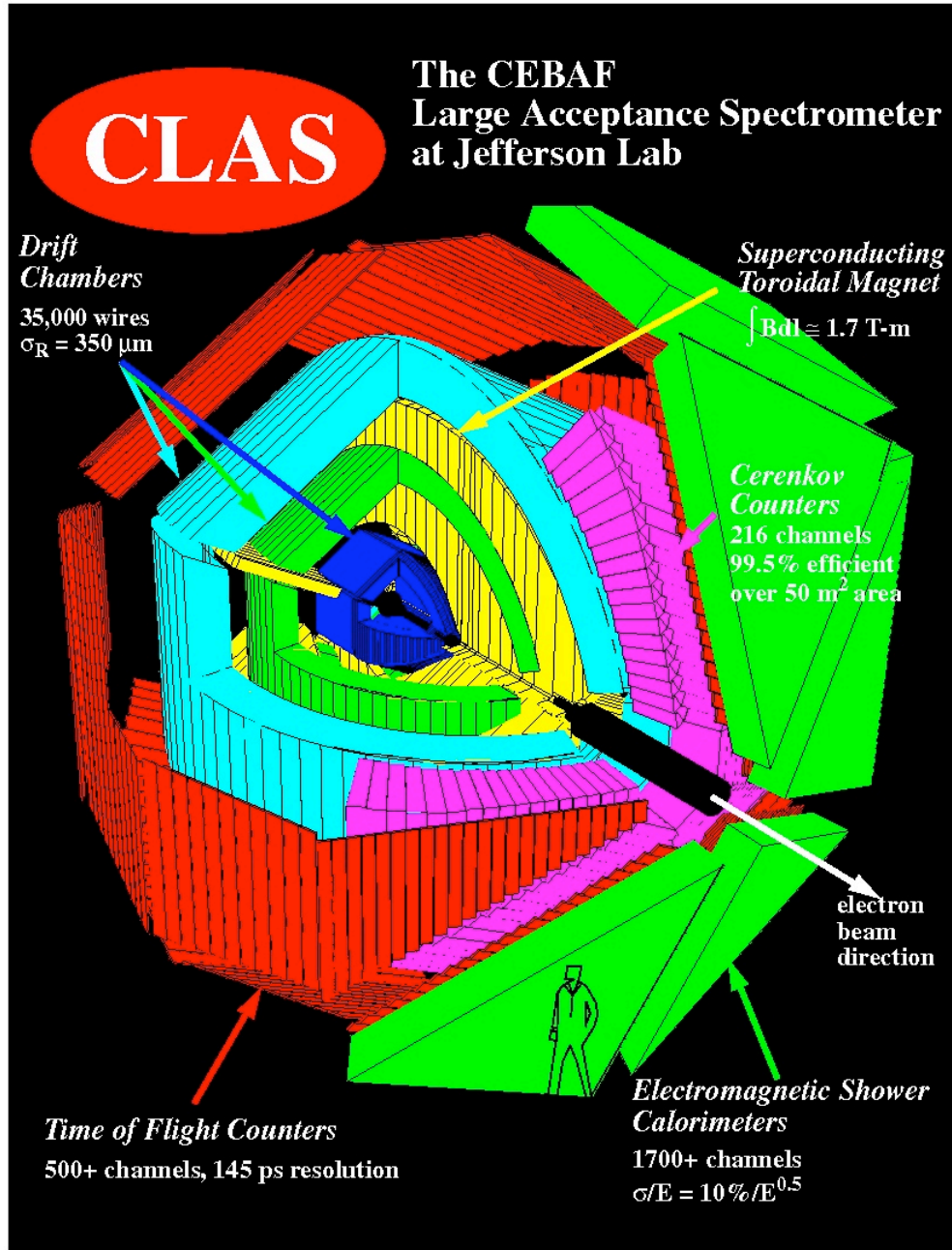
Fig. 2.6: The CEBAF Large Acceptance spectrometer.
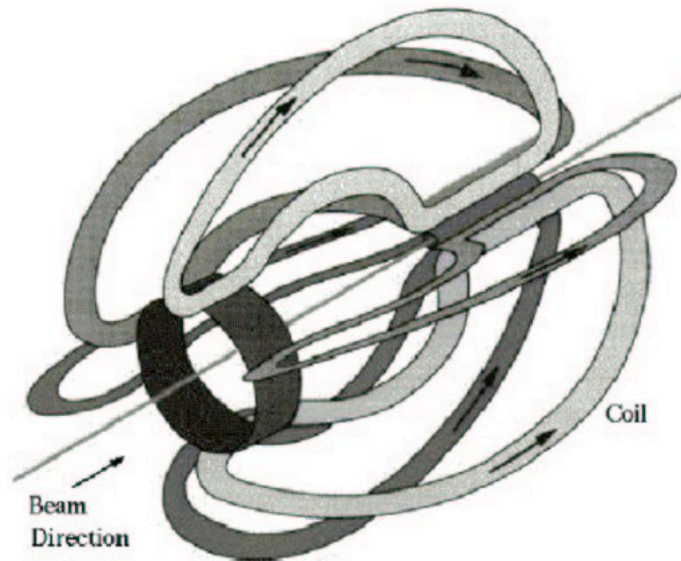
Fig. 2.7: CLAS Torus Magnet.

2.2.3 Drift Chambers

The drift chamber system in the CLAS is divided into three regions, each consisting of six separate chambers (sectors). The drift chambers contain three types of wires stretched between the endplates: sense, guard and field. The end plates are attached to the drift chamber so that the angle they form is equal to 60 (360/6) degrees. Each drift chamber is subdivided into two separate superlayers. Each superlayer has six layers of drift cells. Each drift cell has one sense wire and is surrounded by six field wires forming a hexagonal shape. Each superlayer is surrounded by guard wires at a positive potential to complete the cell symmetry establishing a radial electric field within the drift cells. The sense (field) wire is operated at positive (negative) potential. In each superlayer the distance between the sense and field wire increases with the radial distance from the target. In $R1$ the average distance between the sense and field is 0.7 cm, in R2 1.15 cm, and in R3 2.0 cm [22]. The CLAS drift chamber gas is a 90 - 10 %

mixture of the argon (Ar) and CO_2, where Ar has an ionization gain of $\approx 10^4$.
Inside the drift chamber, a constant pressure is provided by outflowing the gas.
The chamber end plates have a circuit board with a single channel differential
pre-amplifier for each sense wire.

The drift chamber system is used to track charged particles. A drift chamber is
a particle tracking detector that measures the drift time of liberated electrons
in a gas to calculate the spacial position of the ionizing particle with respect to
the sense wire producing the signal.
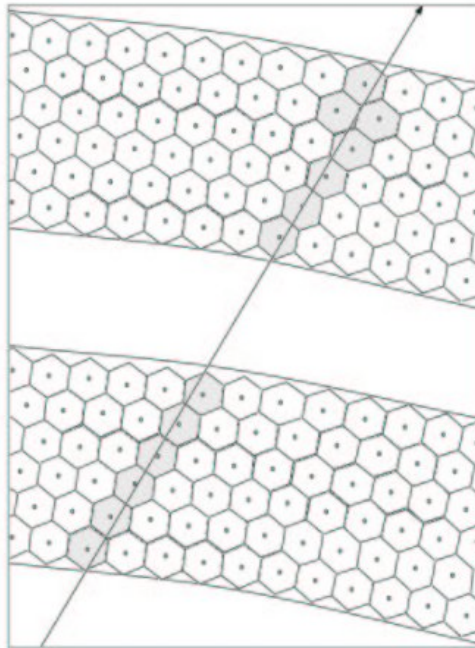
Fig. 2.8: A charged particle passing through two superlayers of the drift chamber.

An electric field in a drift chamber is produced by the anode (sense) and cathode
(field) wires. A charged particle traveling through the drift chamber ionizes the
gas, freeing electrons that are accelerated to the anodes. After a drift time (δt),
electrons are collected at the anode (sense wire) generating a pulse for the time

39

measurement. The distance of the traversing particle from the known position of the sense wire can be calculated using the drift time and drift velocity.

2.2.4   Cherenkov detector

The threshold CLAS Cherenkov detector is used to distinguish electrons from pions. The gas mixture used to fill the Cherenkov counter is perfluorobutane C_4F_{10} gas at atmospheric pressure. The advantage of perfluorobutane C_4F_{10} is its high index of refraction n = 1.00153, which results in a high photon yield. The threshold for Cerenkov radiation can be written as $v > c/n$, or for energies $E > \gamma \times m$, where v is the charged particle velocity, n the index of refraction for the medium, c the speed of light and $\gamma = \frac{1}{\sqrt{1-\frac{1}{n^2}}}$. In our case $\gamma = 18.098$. Accordingly, one can calculate the energy threshold for different charged particles; for electrons it is 9 MeV and for pions 2.5 GeV. The Cherenkov detector was designed to maximize the coverage in each of the sectors up to an angle $\theta = 45$ degrees [23] .

Light is collected using a system of mirrors to focus the light onto cones, which are connected to the Phillips XP4500B type photomultiplier tubes (PMTs). In the extreme regions of the spectrometer's angular acceptance, the number of detected photoelectrons is too low. Additional photomultiplier tubes were placed in these regions to compensate for the low photoelectron detection efficiency.

2.2.5   Scintillators

The CLAS is equipped with 288 scintillator counters. The scintillators are used to determine the time of flight for a charged particle and to determine
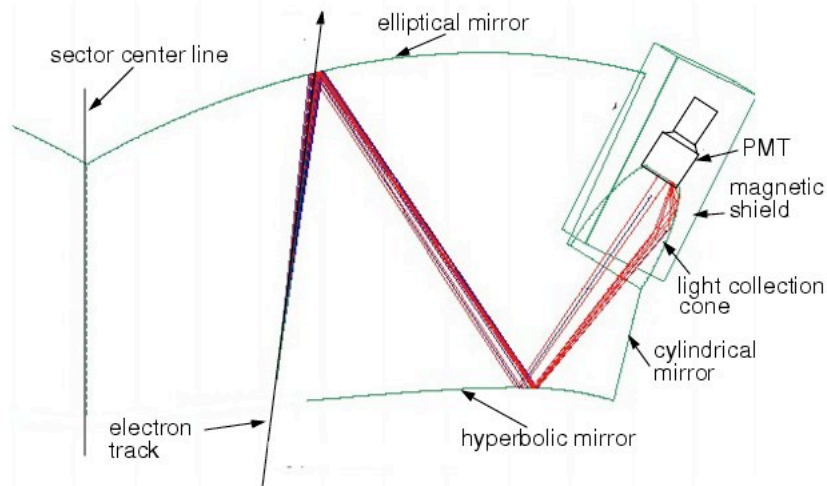
Fig. 2.9: One module of the Cherenkov Counter.

coincidences between particles. The time of flight system has a time resolution at small polar angles of $\Delta t = 120$ ps and $\Delta t = 250$ ps at angles above 90 degrees. This time resolution helps discriminate between pions and kaons up to 2 GeV/c. The time of flight system is located between the Cherenkov detectors and the electromagnetic calorimeters. The scintillator paddles, made from BC_408 [23], are located perpendicular to the average particle trajectory, and have an angular polar coverage of 1.5 degrees each. Each sector of the CLAS consists of 48 scintillator paddles with a thickness of 5.08 cm. The length of the scintillators varies from 30 cm to 450 cm and the width is between 15 cm at small polar angles and 22 cm for the large angles [24].
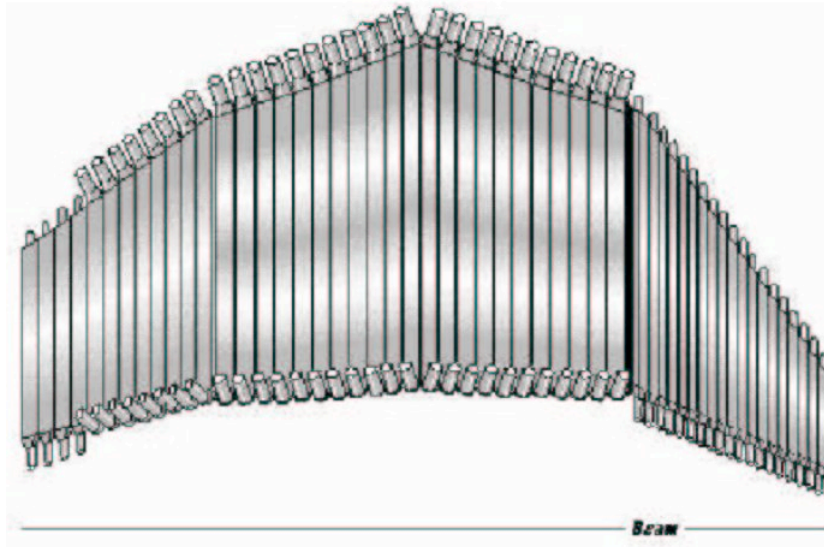
Fig. 2.10: Time-of-Flight system for CLAS.

2.2.6 Calorimeter

The CLAS contains eight electromagnetic calorimeter modules. A calorimeter measures the total energy deposited by a particle that enters the detectors acceptance. Calorimeters are sensitive to neutral particles with sufficient energy to produce secondary particles (referred to as a shower) that can be used to distinguish between the energy deposited by electrons and hadrons. The CLAS calorimeter has three main functions:

- Detection of electrons at energies above 0.5 GeV;

- Detection of photons with energies higher than 0.2 GeV;

- Detection of neutrons, with discrimination between photon and neutrons using time-of-flight techniques.
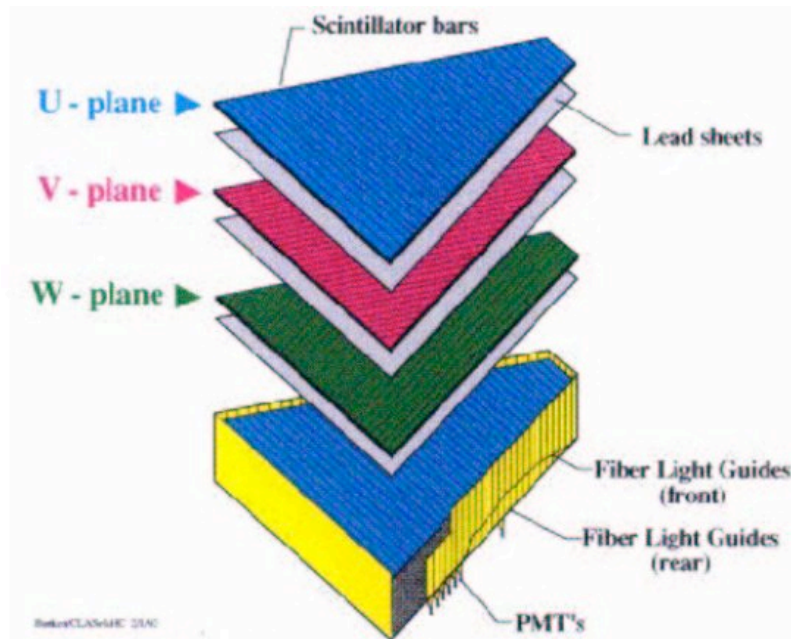
Fig. 2.11: One module of electromagnetic calorimeter.

Calorimeter detectors are placed in the forward region of each sector that span polar angles of $10 - 45$ degrees. Two additional calorimeters are located in sectors 1 and 2 that span polar angles of 50 to 70 degrees. The forward calorimeter has a lead/scintillator thickness ratio of 0.2, with 40 cm of scintillators and 8 cm of lead per module. The lead-scintillator sandwich is shaped to form an equilateral triangle in order to match the hexagonal geometry of the CLAS. Each scintillator layer contains 36 paddles parallel to one side of the triangle, with this configuration each orientation is rotated by 120 degrees from each other. This gives three views, each containing thirteen layers providing stereo information locating the energy deposition. There is a longitudinal sampling of the shower to improve hadron identification. Each set of thirteen layers is subdivided into five inner layers and eight outer layers.

43

2.3 The Continuous Electron Beam Accelerator Facility (CEBAF) at JLAB

The Continuous Electron Beam Accelerator Facility (CEBAF) at the Thomas Jefferson National Accelerator Facility (JLab) contains two 0.5 GeV linacs connected by five sets of recirculated arcs and a 45 MeV polarized electron beam injector with a transverse emittence of less than π mm-mrad and a longitudinal emittence of less than 15π keV-degrees. In order to minimize the total accelerator circumference, the accelerator structure was arranged in two separate linac segments. Each linac segment contains twenty five cryomodules that house eight superconducting radio-frequency cavities. Each cryomodule is seperated by a vacuum port, beam diagnostics, and quadrupole and dipole magnets. Quadrupole and dipole magnets are used to focus and steer the beam. Electrons are accelerated by electric fields within niobium cavities that have been cooled to 2 K using liquid Helium. The field within the cavities is created by klystrons that propagate radio frequency waves through wave guides to the accelerating cavities [25].

A Klystron is a microwave amplifier used to generate electromagnetic waves that are transported by a waveguide from the Klyston to the niobium cavity. The electromotive force (EMF) induced in the RF cavity is roughly parallel to the beam axis and decaying to zero radially at the walls. The EMF induces charge on the interior surfaces of the cavities such that the electrons moving through the cavity see a positive charge in front of them and accelerate towards
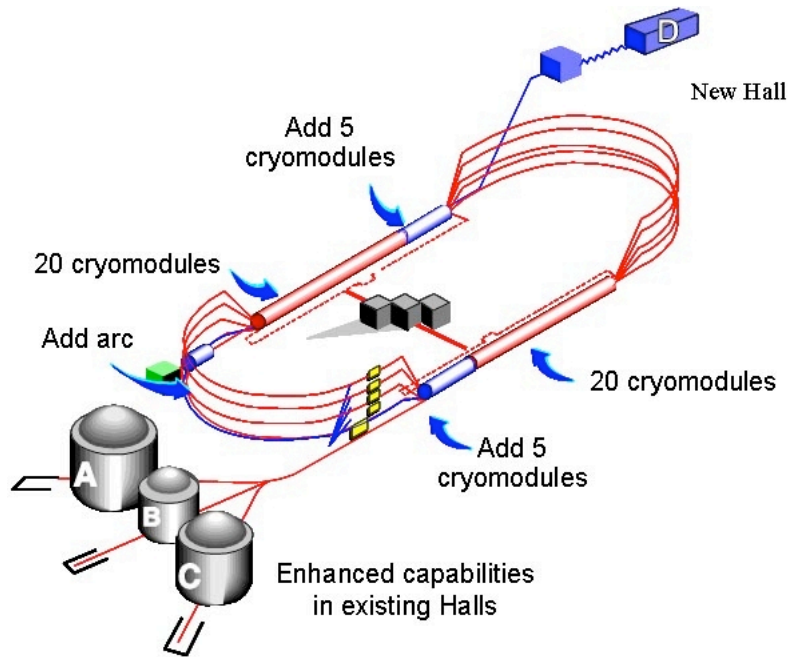
Fig. 2.12: CEBAF 12 GeV upgraded accelerator.

that charge. As a result, the klyston establishes an electromagnetic wave within the niobum cavity that collects electrons on the crest of the wave into bunches that are spaced by 2.04 ns [26].

After the beam reaches the desired energy it is sent to one of the three Halls using an RF kicker at the switch yard. This allows the Halls to receive separate energies.

Polarized electron beams are created at JLab using a GaAs photocathode. The polarized electrons are produced by bandgap photoemission from a strained GaAs cathode using a tunable Ti-Saphire laser having wavelengths from 780 to 850 nm with at least 500 mWatts of output power [27]. When the cathode is exposed to circularly polarized laser light, polarized electrons move from the valence region to the conduction band. In order to free the electrons from the conduction band, the surface of the GaAs cathode is coated with a single layer

45

Quantity	Value
Electron beam energy E (GeV)	$0.8 \leq E \leq 6.0$
Max Electron beam current in one Hall(μAmp)	100
Energy spread ($\Delta E/E$)	10^{-4}
Electron beam polarization	40-80%
Simultaneous beams	3
Number of linac segments	2
Number of passes	4
Maximum energy gain per pass (GeV)	1.5

Table 2.1: The CEBAF accelerator parameters [25].

of cesium and fluorine. As a result, electrons in the conduction band are bound to the surface of the material by only 4 eV. For the EG1b experiment, the sign of the electron polarization was flipped with a frequency of 1 Hz by reversing the laser polarization with a pseudo-random sequence. The electron beam polarization for each hall can be changed with a Wien Filter, which can rotate electron spin without changing its direction [28].

The electron beam quality during the experiment is monitored with several devices: Mott polarimeter, Moller polarimeter, Faraday cup and harp scan. The beam polarization is measured using a 5 MeV Mott polarimeter at the injector and a Moller polarimeter in Hall B, which is located upstream to the target position. The average electron beam polarization during the EG1b experiment was measured by the Hall B moller polarimeter to be $(70 \pm 5)\%$ [29]. The integrated electron beam current is measured using a Farady cup located downstream of the CLAS target. It contains several layers of lead and scintillator in order to create a large amount of detected secondary particles from the primary electron beam. The position of the beam is measured using beam position monitors. The profile of the beam is monitored with a harp scan, a

device with thin iron and tungsten wires that measures the beam charge when swept through the beam.

CHAPTER 3
Data Analysis

This chapter describes the techniques used to analyze the data collected during the EG1b experiment and calculate semi-inclusive cross sections for the following reactions: $\vec{e}^- \vec{N} \rightarrow e^- \pi^+ X$ and $\vec{e}^- \vec{N} \rightarrow e^- \pi^- X$ using NH_3 and ND_3 polarized targets respectively. The goal of this work is to measure charged pion asymmetries defined according to the incident electron helicity and the target polarization. The measured asymmetries may be used to determine if the fragmentation function is independent of the observed final state hadron fractional energy (z) [12]. The quantity $(\Delta R_{np}^{\pi^+ + \pi^-})$ is defined in terms of the ratio of the difference of polarized semi-inclusive deep inelastic scattering cross sections for proton and neutron targets to unpolarized cross sections:

$$\Delta R_{np}^{\pi^+ + \pi^-} = \frac{\Delta \sigma_p^{\pi^+ + \pi^-} - \Delta \sigma_n^{\pi^+ + \pi^-}}{\sigma_p^{\pi^+ + \pi^-} - \sigma_n^{\pi^+ + \pi^-}}. \tag{3.1}$$

A measure of ΔR can be used to test for independent fragmentation when it is compared to inclusive structure functions as shown in Eq. (1.54).

3.0.1 The CLAS Data Selection

The data files from the EG1b experiment chosen for this analysis are listed in Table 3.1. During the experiment, 2.2 GeV, 4.2 GeV and 5.7 GeV longitudinally

polarized electron beams were used to probe the polarized frozen ammonia NH_3 and ND_3 targets. This work will discuss the analysis of the 4.2 GeV energy electron beam data set as this energy provided the most statistics. The collected data have been tested by applying restrictions discussed later in this chapter.

Run Set	Target Type	Torus Current(A)	Target Polarization	HWP
28100 - 28102	ND_3	+2250	-0.18	+1
28106 - 28115	ND_3	+2250	-0.18	-1
28145 - 28158	ND_3	+2250	-0.20	+1
28166 - 28190	ND_3	+2250	+0.30	+1
28205 - 28217	NH_3	+2250	+0.75	+1
28222 - 28236	NH_3	+2250	-0.68	+1
28242 - 28256	NH_3	+2250	-0.70	-1
28260 - 28275	NH_3	+2250	+0.69	-1
28287 - 28302	ND_3	-2250	+0.28	+1
28306 - 28322	ND_3	-2250	-0.12	+1
28375 - 28399	ND_3	-2250	+0.25	-1
28407 - 28417	NH_3	-2250	+0.73	-1
28456 - 28479	NH_3	-2250	-0.69	+1

Table 3.1: EG1b runs analyzed for this work.

3.1 Particle Identification

Additional tests were performed on the electron and a pion candidates reconstructed using the standard CLAS software package on the raw data collected during the EG1b experiment. Electrons are identified by matching the charged particle hits in the Cherenkov counter, electromagnetic calorimeter, and Time of Flight system. Geometrical and timing cuts are applied to improve electron identification. In addition, cuts are applied on the energy deposited by the

particle into the calorimeter and the number of photoelectrons produced in the Cherenkov counter. Charged pions are identified by matching the hits in the drift chamber and ToF counter, along with a Cherenkov cut requiring that the number of photons for pions be less than two.

3.1.1 Electron Identification

The CLAS trigger system required the particle to deposit energy in the electromagnetic calorimeter and illuminate the Cherenkov counter within a 150 ns time window (Figure 3.1). Unfortunately, this trigger suffers from a background of high energy negative pions that may be misidentified as electrons. The pion contamination of the electron sample is reduced using cuts on the energy deposited in the electromagnetic calorimeter and the momentum measured in the track reconstruction for the known magnetic field. The energy deposition mechanism for the pions and electrons in the electromagnetic calorimeter is different. The total energy deposited by the electrons in the EC is proportional to their kinetic energy, whereas pions are minimum ionizing particles and the energy deposition is independent of their momentum (Figure 3.2). The pion background is further suppressed using geometrical and time matching between the Cherenkov counter hit and the measured track in the drift chamber.

EC CUTS

The CLAS electromagnetic calorimeter was used to reduce the misidentification of electron and negative pion candidates. The electromagnetic calorimeter contains thirteen layers of lead-scintillator sandwiches composed of ~ 2 mm thick
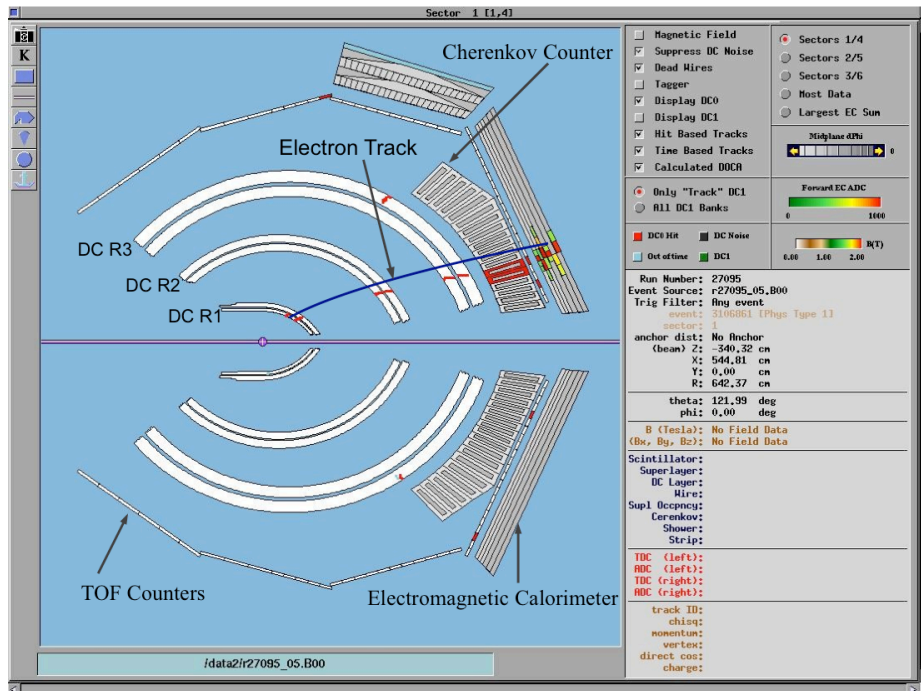
Fig. 3.1: Example of electron passing through the drift chambers and creating the signal in the Cherenkov counter and electromagnetic calorimeter. Electron track is highlighted by the blue line (Run number 27095, Torus Current +2250 (inbending)).

lead and 10 mm thick scintillator. Each set of thirteen layers are subdivided into five inner and eight outer layers that are named the inner and outer calorimeter respectively. Electrons interact with the calorimeter producing electromagnetic showers that release energy into the calorimeter. The deposited energy is proportional to the momentum of the electrons. Figure 3.3 shows the correlation of the inner and outer calorimeter electron candidate's energy measured by the calorimeter and divided by the particles momentum reconstructed by the drift chamber. As shown in the Figure 3.3, there is an island near $E/p = 0.2$, which contains most of the electron candidates as well as some regions below 0.2 which will be argued to be negative pions misidentified as electrons.

Pions entering the calorimeter are typically minimum ionizing particles, loos-
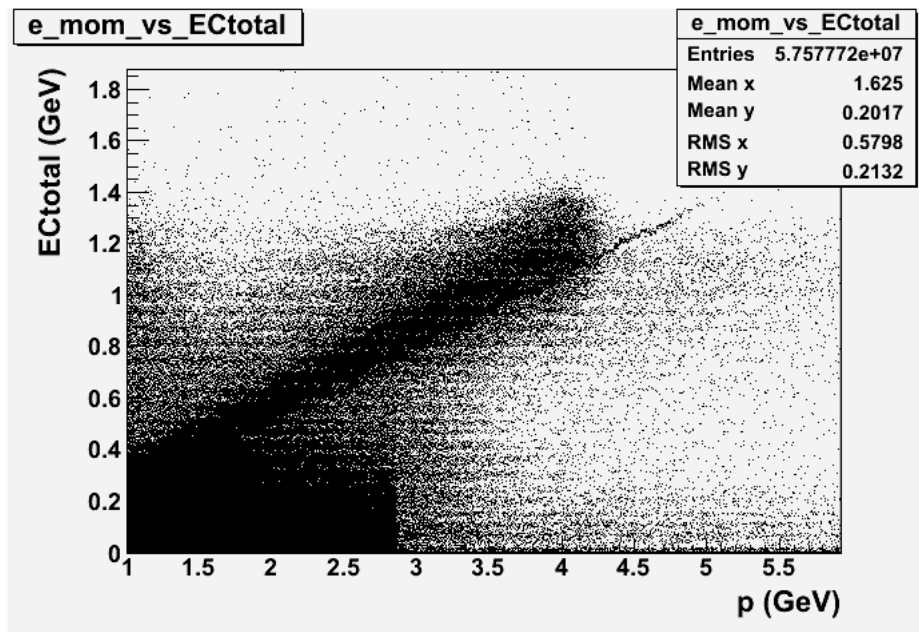
Fig. 3.2: Momentum versus ECtotal.

ing little of their incident energy in the calorimeter at a rate of 2 MeV g^{-1}cm^2. Electrons, on the other hand, deposit a larger fraction of their momentum into the calorimeter. As a result, the energy deposited into the electromagnetic calorimeter is different for electrons and pions. Pions loose about 0.08 GeV of energy traversing the calorimeter independent their momentum thereby producing the constant signal in the calorimeter around 0.08 GeV. In order to reduce misidentified pions from the electron sample, the following cut has been applied:

$$EC_{inner} > 0.08 \times p, \qquad (3.2)$$

where p represents particle momentum and EC_{inner} the inner part of the calorimeter.

Since the energy loss of pions is related to the calorimeter thickness, a correla-

tion can be established between the energy deposited into the inner and outer layers of the calorimeter:

$$\frac{EC_{tot}}{EC_{inner}} = \frac{13}{5},$$

(3.3)

which gives the following cut for the energy deposition into the outer layer of the calorimeter:

$$EC_{tot} > 0.2 \times p.$$

(3.4)

Cherenkov Counter Cut

The Cherenkov counter has been used to further reduce the negatively charged pion background in the reconstructed electron sample. When the velocity of a charged particle is greater than the local phase velocity of light or when it enters a medium with different optical properties, the charged particle will emit photons. Cherenkov light is emitted at the critical angle θ_c representing the angle of Cherenkov radiation relative to the particle's direction. It can be shown that the cosine of the Cherenkov radiation angle is inversely proportional to the velocity of the charged particle

$$\cos\theta_c = \frac{1}{n\beta},$$

(3.5)

where βc is the particle's velocity and n the index of refraction of the medium. The charged particle in time t travels a distance $\beta c t$, while the electromagnetic waves travel $\frac{c}{n}t$. For a medium with given index of refraction n, there is a threshold velocity $\beta_{thr} = \frac{1}{n}$, below which no radiation is emitted. This process may be used to distinguish between the highly relativistic electrons and the less
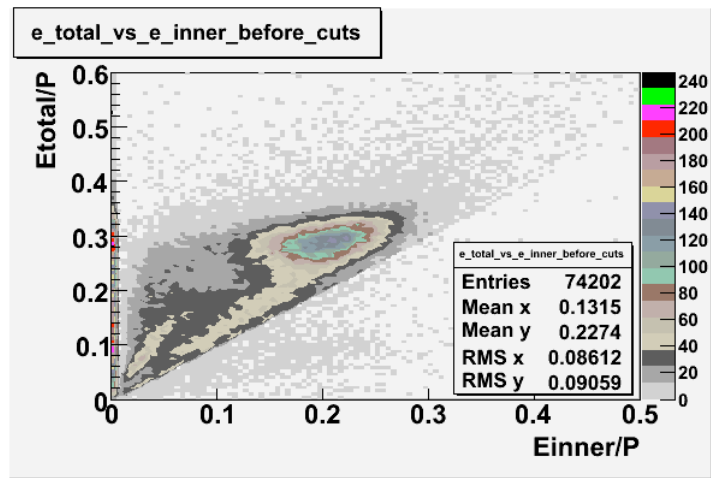
(a) Before cuts.
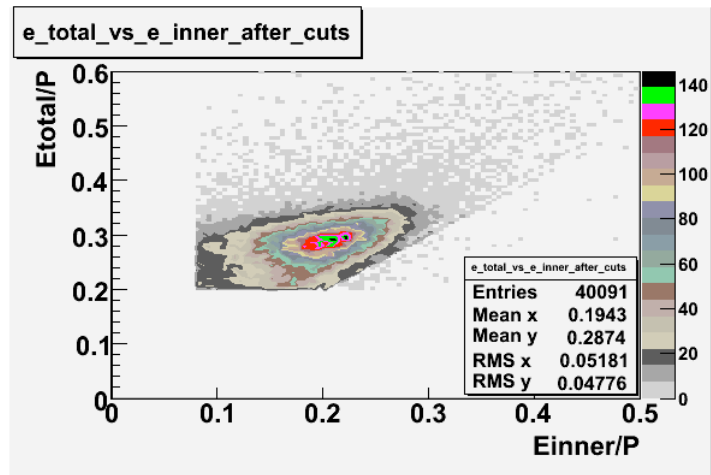
(b) After cuts.

Fig. 3.3: EC_{inner}/p versus EC_{tot}/p before and after EC cuts ($EC_{tot} > 0.2p$ and $EC_{inner} > 0.08p$). After applying EC cuts about 46% of the events have been removed from the electron sample.

relativistic pions based on the number of photons produced. The number of photons produced per unit path length of a particle with charge Ze and per unit energy interval of the photons is proportional to the sine of the Cherenkov angle [31]

$$\frac{d^2N}{dEdx} = \frac{\alpha z^2}{\hbar c} \sin^2 \theta_c = \frac{\alpha z^2}{\hbar c} \left[1 - \frac{1}{\beta^2 n^2(E)} \right] \qquad (3.6)$$

$$\frac{d^2N}{d\lambda dx} = \frac{2\pi\alpha z^2}{\lambda^2}[1 - \frac{1}{\beta^2 n^2(\lambda)}] \qquad (3.7)$$

$$\beta = \frac{v}{c} = \frac{pc}{\sqrt{(pc)^2 + (mc^2)^2}}. \qquad (3.8)$$

Taylor expanding Eq. 3.6 and keeping only the first two terms we get following

$$\frac{d^2N}{dEdx} = \frac{\alpha z^2}{\hbar c}\sin^2\theta_c = \frac{\alpha z^2}{\hbar c}[\beta^2 n^2(E) - 1]. \qquad (3.9)$$

The gas used in the CLAS Cerenkov counter is perfluorobutane C_4F_{10} with index of refraction equal to 1.00153. The number of photoelectrons emitted by electrons is about thirteen. On the other hand, calculations show that the number of photons produced by the negatively charged pions in the Cherenkov detector is approximately 2. The theoretical results of the number of photons produced by the electrons and pions when passing through the Cherenkov counter are shown on Figure 3.4.

The distribution of the number of photoelectrons measured in the Cherenkov detector and the energy deposition dependence on number of photoelectrons are shown on Figure 3.5 and Figure 3.6. One can see that a single photoelectron peak is caused by misidentifying pions as electrons.

Geometric and Timing cuts

Negative pions may be produced when the lepton scatters at a polar angle close to zero and is not observed by the detector. In order to reduce the electron sample contamination due to those pions, geometrical cuts on the location of
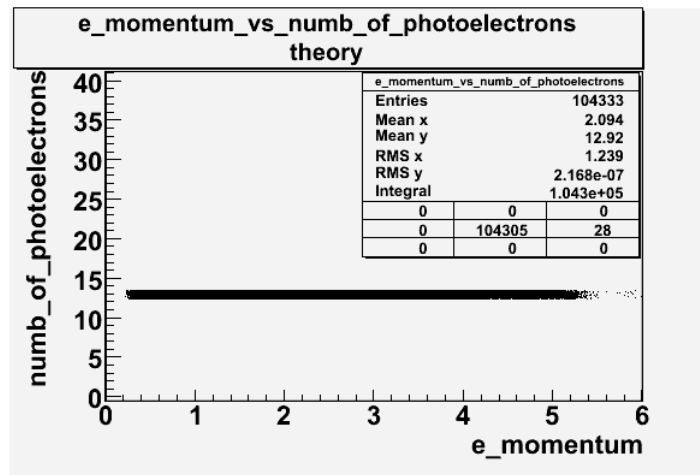
(a) For electrons.
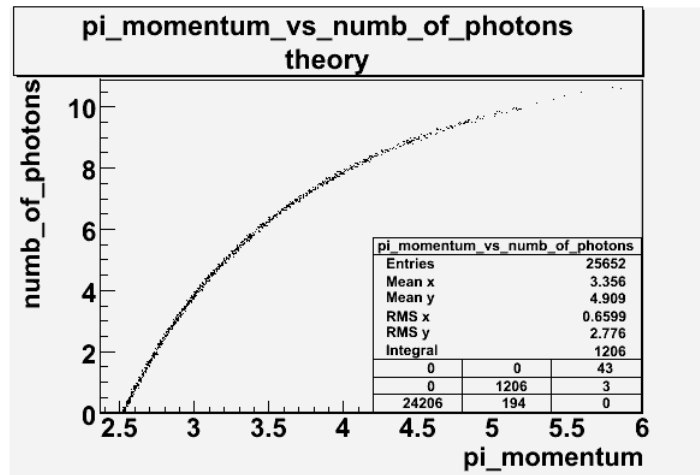
(b) For pions.

Fig. 3.4: Theoretical Calculation of the Number of Photoelectrons for electrons and pions.

the particle at the entrance to the Cherenkov detector and time matching cuts have been developed by Osipenko, so called OSI cuts [32]. For each CLAS Cherenkov detector segment the following cut has been applied

$$|\theta_p - \theta_p{}^{center} - \theta_p{}^{offset}| < 3\sigma_p, \tag{3.10}$$

56
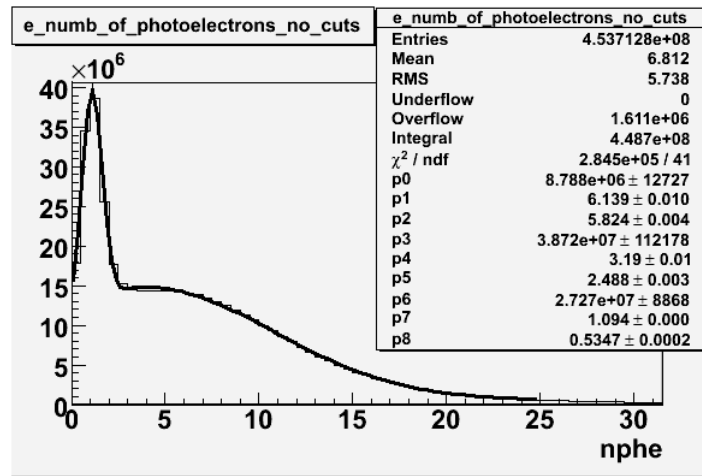
Fig. 3.5: The number of photoelectrons without cuts.
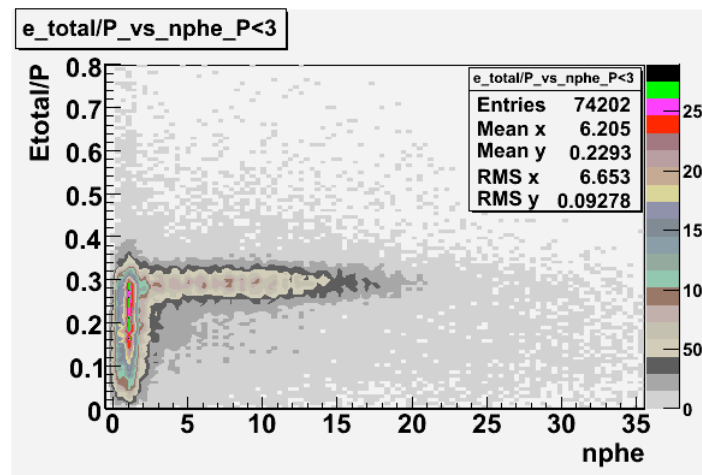
Fig. 3.6: The total energy deposited into the Calorimeter versus the Number of Photoelectrons.

where θ_p represents the measured polar angle with respect to a projectile plane for each electron event. The Cherenkov counter's projective plane is an imaginary plane behind the Cherenkov detector where Cherenkov radiation would have arrived if it had moved the same distance from emission point to the PMT, without reflections in the mirror system. θ_p^{center} is the polar angle from the CLAS detector center to the image of Cherenkov counter segment center

57

and $\theta_p{}^{offset}$ is the shift in the segment center position. In addition to geometrical cuts, timing cuts have been applied to match the time between a Cherenkov counter hit and time of flight system.

The pion contamination in an electron sample was estimated by fitting the number of photoelectron distribution using two Gaussian distributions convoluted with a Landau distribution [33]:

$$N_{pe} = p_0 e^{-0.5\left(\frac{x-p_1}{p_2}\right)^2} + p4 \frac{1}{1-\left(\frac{x-p5}{p6}\right)} + p_6 e^{-0.5\left(\frac{x-p_7}{p_8}\right)^2}. \qquad (3.11)$$

The fits in Figure 3.7.(a) suggest that the pion contamination in the electron sample is $9.63\% \pm 0.01\%$ before applying the OSI cuts and after the OSI cuts the contamination is about $4.029\% \pm 0.003\%$ (Figure 3.7.(b)).

3.1.2   Pion Identification

Charged pions are identified using a coincidence hit in the drift chamber and Time-of-Flight (ToF) counter. Pions are separated from the other charged particles by looking at the particle momentum versus the β distribution. The particle velocity, $\beta = \frac{v}{c}$, is calculated from the difference of the RF time and the time-of-flight measurement in the ToF system with the path length from the vertex to the ToF counters. The mass of the charged particle can be identified by combining the particle's β with the particle momentum obtained from the track measured by the drift chamber in the known magnetic field. The particle
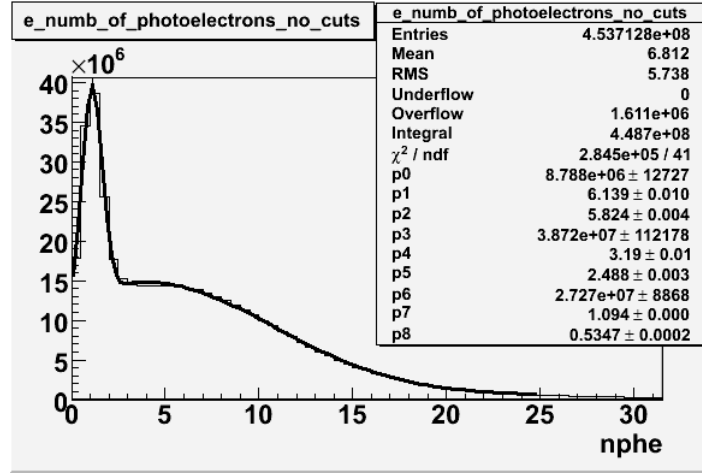
(a) Before Cuts.
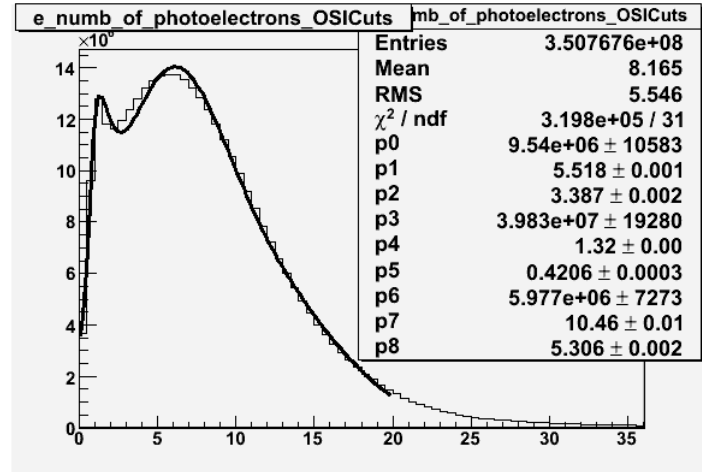
(b) After OSI Cuts.

Fig. 3.7: The number of photoelectrons before and after geometrical and time matching cuts.

mass in a magnetic field is given as

$$p = \frac{m\beta}{\sqrt{1-\beta^2}} \tag{3.12}$$

$$m = p\sqrt{(\beta^2 - 1)} \tag{3.13}$$

$$\beta = \frac{L_{path}}{t_{flight}}, \tag{3.14}$$

59

where m is the mass of the charged particle, β its velocity, p particle momentum, L_{path} the path length from the vertex to scintillators and t_{flight} the time of flight from the interaction vertex to the ToF system.

Using the above information (particle momentum from the drift chambers and the timing information from the ToF system), the mass squared of the charged particle was calculated and is shown on Figure 3.9. The pion mass band is around ~ 0. To isolate charged pions from the rest of the particles, a 3σ cut on the momentum versus β distribution has been applied [34].
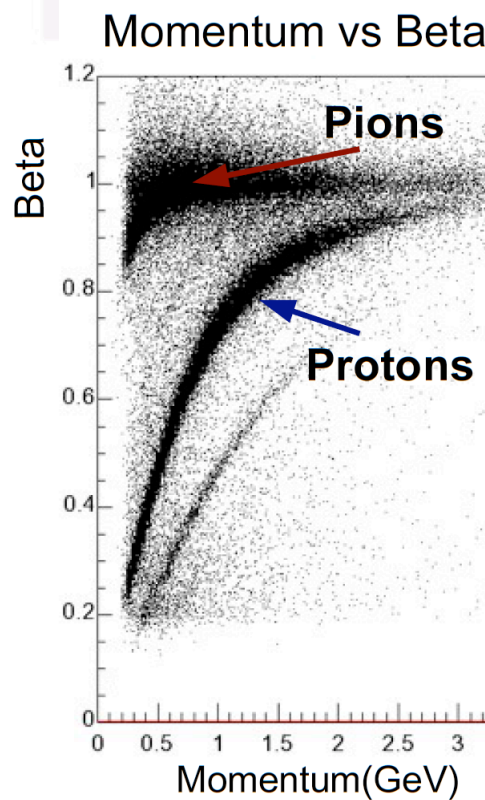
Fig. 3.8: The charged particle momentum versus β distribution. The pion and proton bands are clearly separated.
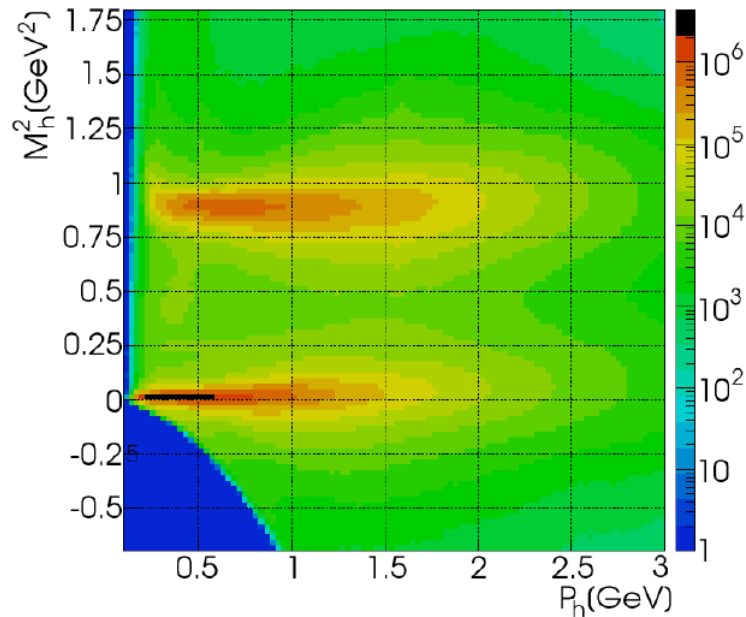
Fig. 3.9: The charged particle momentum versus mass squared distribution for the $\overrightarrow{e}p \rightarrow \overrightarrow{e}'\pi^+ n$ electroproduction process. The bands around 0 and 1 represent pions and protons respectively [34].

In addition to the charged particle velocity (β), the fiducial volume cuts have been applied for the charged pion identification. Since the drift chambers and scintillators are used for pion detection, the polar angle range where pions are detected is much larger than for electrons. For the EG1b experiment, pions were detected from 8° to 180° [34]. The pion identification code has been developed by Joshua Pierce [35].

3.2 Event Reconstruction Efficiency

The goal of this work is to measure the semi-inclusive asymmetry when an electron and a pion are detected in the final state. For this analysis, pions of opposite charge will be observed using the same scintillator paddles by flipping

the CLAS torus magnetic field direction. Although the pions will be detected by the same detector elements, the electrons will intersect different detector elements. As a result, the electron reconstruction efficiency was evaluated in terms of the electron rate observed in two different scintillator paddles detecting the same electron kinematics.

3.2.1 Inclusive Electron Event Reconstruction Efficiency

The electron reconstruction efficiency for individual scintillator detectors using the 4.2 GeV EG1b data is investigated below. Only the electron is detected in the final state (inclusive case). The pion contamination in the electron sample was removed by applying the cuts described above. The electron paddle numbers 10 (B<0) and 5 (B>0) were chosen respectively, because they contained the most electron events in a first pass semi-inclusive pion analysis of the data set. The electron kinematics (momentum, scattering angle and invariant mass) for these scintillators is shown on Figure 3.10.

Ratios of the inclusive electron rate, normalized using the gated Faraday cup, detected in scintillator paddles # 5 and # 10 were measured. The two ratios are constructed to quantify the CLAS detector's ability to reconstruct electrons in scintillator paddle #5 using a positive Torus polarity and scintillator #10 using the negative Torus polarity.

$$\frac{ND_3, B > 0, PaddleNumber^{e^-} = 5}{ND_3, B < 0, PaddleNumber^{e^-} = 10} = 1.57 \pm 0.16 \qquad (3.15)$$

$$\frac{NH_3, B > 0, PaddleNumber^{e^-} = 5}{NH_3, B < 0, PaddleNumber^{e^-} = 10} = 1.76 \pm 0.17. \qquad (3.16)$$

Notice the above ratios are statistically the same. The semi-inclusive analysis to be performed in this thesis will be taking ratios using an ND_3 and NH_3 target. Below is the observed ratio comparing the inclusive electrons observed in scintillator #5 for a positive torus polarity and an ND_3 target to the electrons observed in scintillator #10 when the torus polarity is negative and the target is NH_3.
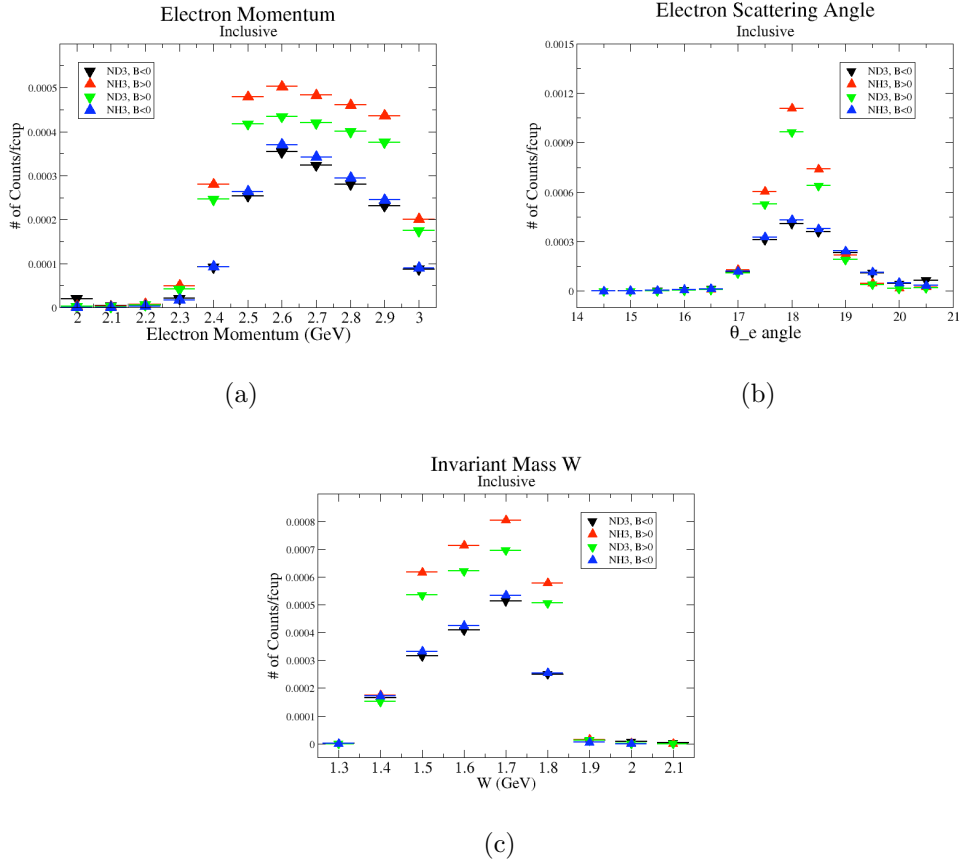
Fig. 3.10: Electron Kinematics. (a) Electron Momentum((NH_3,B>0), (NH_3,B<0), (ND_3,B>0) and (ND_3,B<0)), (b) Electron Scattering Angle θ ((NH_3,B>0), (NH_3,B<0), (ND_3,B>0) and (ND_3,B<0)) and (c) W Invariant mass((NH_3,B>0), (NH_3,B<0), (ND_3,B>0) and (ND_3,B<0))

$$\frac{ND_3, B > 0, PaddleNumber^{e^-} = 5}{NH_3, B < 0, PaddleNumber^{e^-} = 10} = 1.55 \pm 0.15. \tag{3.17}$$

The above ratios, which have been observed to be ammonia target independent, indicate a difference in an electron detector efficiency when the torus polarity is flipped. An electron detection efficiency "correction coefficient" is defined in terms of the above ratio and measured to be $\frac{ND_3, B>0, E_{PaddleNumber}=5}{NH_3, B<0, E_{PaddleNumber}=10} = 0.645$ and $\frac{ND_3, B<0, E_{PaddleNumber}=10}{NH_3, B>0, E_{PaddleNumber}=5} = 1.82$. The impact of these corrections on the data is illustrated in the next section.

3.2.2 Exclusive and Semi-Inclusive Event Reconstruction Efficiencies

After determining the electron reconstruction efficiency for the selected paddle numbers, the measured single pion electroproduction rate was compared to the MAID 2007 unitary model that has been developed using the world data of pion photo and electro-production to determine the impact of using the above "correction coefficient". The model is well adopted for predictions of the observables for pion production, like five fold cross section, total cross section, etc.

The MAID 2007 model has predictions of the total cross section for the following two cases that are related to our work:

$$\gamma^* + \text{proton}(\text{NH}_3) \rightarrow \pi^+ + \text{neutron} \tag{3.18}$$

$$\gamma^* + \text{neutron}(\text{ND}_3) \rightarrow \pi^- + \text{proton}. \tag{3.19}$$

The ratio of the pions detected in the scintillator paddles, located between the

Cherenkov counter and electromagnetic calorimeter, is shown in Figure 3.11. The ratios were taken for four different cases. The intrinsic assumption is that, for the inbending case, positive pions and for the outbending case negative pions have the same trajectories with the same kinematics. In addition, negatively charged pions in the inbending field and positively charged pions in the outbending fields are detected by the same detector elements.
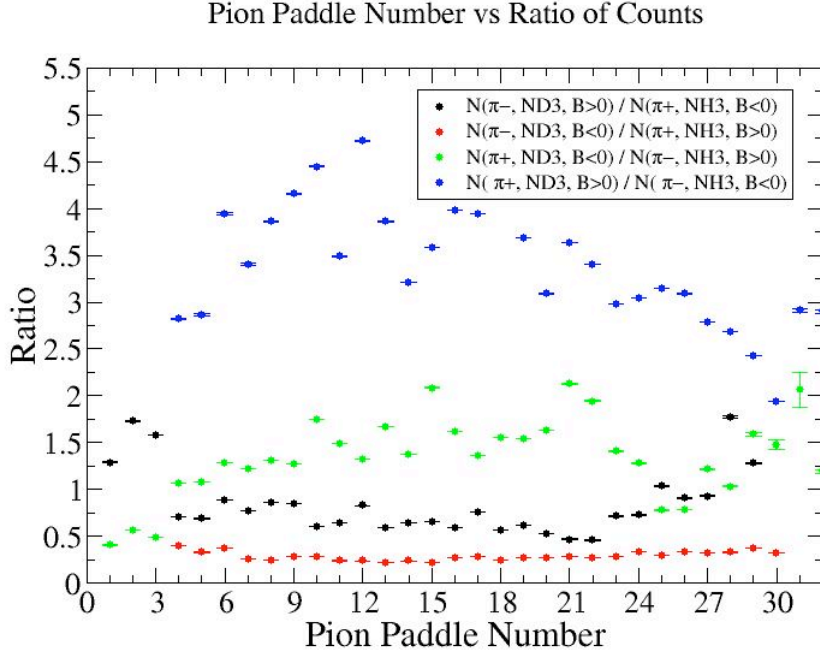
Fig. 3.11: Pion paddle number versus Ratio for Semi-Inclusive case.

Using MAID 2007, the total cross section was calculated for the following invariant mass and four momentum transferred square values: 1.7 GeV < W<1.8 GeV and Q^2=1.1 GeV^2 [36].

$$\sigma = \sigma_T + \epsilon\sigma_L + \sqrt{2\epsilon(1+\epsilon)}\sigma_{LT}\cos\phi_\pi{}^{CM} + +\epsilon\sigma TT\cos 2\phi_\pi{}^{CM} + h\sqrt{2\epsilon(1-\epsilon)}\sigma_{LT'}\sin\phi_\pi{}^{CM},$$

$$(3.20)$$

where $\phi_\pi{}^{CM}$ is the pion azimuthal angle in the CM frame, $\epsilon = (1 + 2(1 + \frac{\nu^2}{Q^2}) \tan^2 \frac{\theta_e}{2})^{-1}$ is the virtual photon polarization, $\nu = E_i - E_f$ the energy difference of the initial and final state electron, $Q^2 = 4E_iE_f \sin^2 \frac{\theta_e}{2}$ the four momentum transferred squared, θ_e the electron scattering angle and h the electron helicity. After applying corrections from the inclusive cases, the ratios have been compared to the results from MAID2007. The difference of the measured and MAID2007 model ratios for each pion paddle number is shown in Figure 3.12. One can conclude from Figure 3.12 that the "inclusive corrections" do not impact single pion production rates for the exclusive cases.

Fig. 3.12: Pion Paddle Number versus MAID2007 - Experiment(N(π^-,ND$_3$)/N(π^+,NH$_3$)). The Black and red data represent B>0/B<0 and B<0/B>0 cases respectively before corrections. The green and blue points represent the ratios for B>0/B<0 and B<0/B>0 after inclusive corrections.

3.3   Asymmetries

The double spin asymmetry measurements in this thesis are performed by comparing scattering events that occur when the incident probe spin and nuclear target spin are parallel to the scattering events that occur when the spins are anti-parallel.

3.3.1   Beam Charge Asymmetry

The helicity of the electron beam was flipped at a rate of 1 Hz. The helicity is prepared at the source such that helicity pairs are produced pseudo randomly.
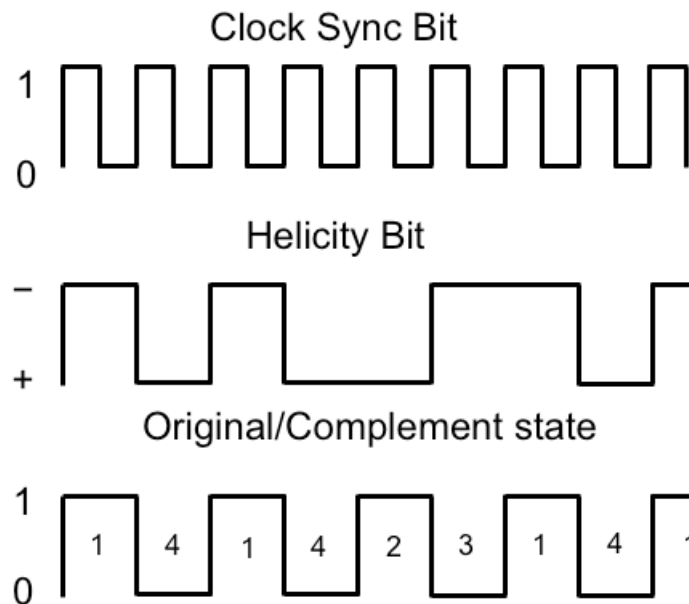
Fig. 3.13: The Helicity State: A one bit signal from the beam injector gives the helicity information, whereas a sync bit with a 2 Hz frequency is generated at the same time and is equal to the helicity flip time.

If the first electron bunch is pseudo randomly chosen to be positive (negative) then it is labeled as the original helicity state and denoted in software by a 2

67

(1). The next helicity state is prepared to be a complement to the first state and labeled in the software as either a 4, if the original helicity state was a 1 (negative), or 3 if the original helicity state was a 2 (positive). The helicity selection process is then repeated.

Figure 3.13 illustrates the signals used to label the helicity states. The clock pulse (SYNC) is used to indicate that a change in the pockel cell used to define the helicity state may have occurred. The helicity bit identifies the helicity state that was set. The original/complement pulse identifies if the state is an original or complement helicity state. All three bits are recorded in the raw data file for each event and then converted to the labels 1, 2, 3, 4 during DST file production once the particles have been reconstructed.

Two scalers were used to record several ancillary detectors, such as a Faraday cup and several PMTs mounted on the beam line, according to their helicity label. One of the scalers was gated by the DAQ live time in order to record beam conditions when the DAQ was able to take data and not busy recording data. The second scaler remained ungated. Both scalers recorded the SYNC and Helicity signals from the injector along with the counts observed from ancillary detectors during the SYNC interval. The Faraday cup signal recorded by the gated helicity scaler is used to normalize the events reconstructed during the same helicity interval. The beam charge asymmetry below is measured by the gated helicity scaler. For each run number, a gaussian fit was used to fit the beam charge asymmetry distributions as in Figure 3.14. The beam charge asymmetry is defined as

$$A_{BeamCharge} = \frac{\Sigma FC^{hel1,hel2} - \Sigma FC^{hel4,hel3}}{\Sigma FC^{hel1,hel2} + \Sigma FC^{hel4,hel3}}, \tag{3.21}$$

where $FC^{hel1,hel2}$ ($FC^{hel4,hel3}$) represents the Faraday cup counts observed for the original helicity 1 and 2 states (the complement helicity 3 and 4 states).
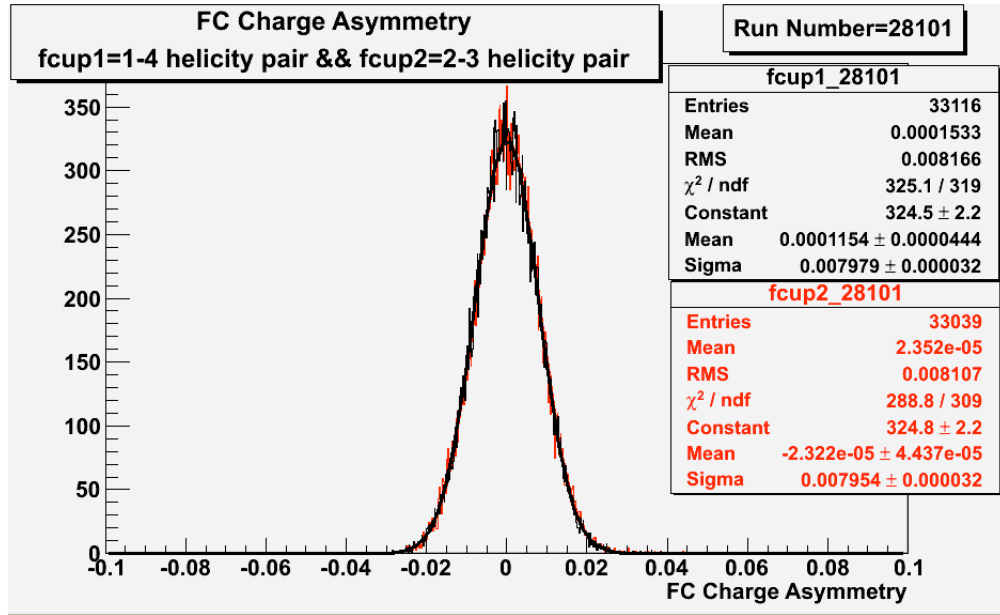
Fig. 3.14: Beam charge asymmetry for run #28101 using the gated Faraday cup counts for two helicity pairs (1-4 and 2-3 helicity pairs). $A_{1-4} = (11.5 \pm 4.4) \times 10^{-5}$ and $A_{2-3} = (-2.3 \pm 4.4) \times 10^{-5}$.

EG1b data sets, with the same half wave plane, target type, target polarization and beam torus, have been combined. The beam charge asymmetries have been calculated for the each run group and are listed in Table 3.2.

3.3.2 Electron Asymmetry

A measurement of the electron cross section helicity difference needs to account for a possible helicity dependence of the incident electron flux (charge Asymmetry). Figure 3.15 shows the reconstructed electron asymmetry before it is normalized by the gated Faraday Cup as a function of the run number for

Run Group	Half wave plane(HWP)	$A_{1-4} \times 10^{-4}$	$A_{2-3} \times 10^{-4}$
$28100 - 28105$	+1	5.88 ± 34.40	4.03 ± 34.36
$28106 - 28115$	-1	7.53 ± 22.30	8.28 ± 22.30
$28145 - 28240$	+1	31.70 ± 7.99	30.40 ± 7.99
$28242 - 28284$	-1	49.6 ± 10.8	47.9 ± 10.8
$28286 - 28324$	+1	36.3 ± 11.6	37.0 ± 11.5
$28325 - 28447$	-1	21.1 ± 13.4	22.2 ± 13.4
$28449 - 28479$	+1	-11.6 ± 16.5	-21.6 ± 16.5

Table 3.2: Run Group versus Beam Charge Asymmetry.

the 4.2 GeV data set. The reconstructed electron asymmetry can be defined following way:

$$A_{NES}^{+-} = \frac{NES^+ - NES^-}{NES^+ + NES^-} \equiv (2-3),$$ (3.22)

or

$$A_{NES}^{-+} = \frac{NES^- - NES^+}{NES^- + NES^+} \equiv (1-4),$$ (3.23)

where NES^+ (NES^-) represents number of electron scattered for the positive (negative) beam helicity.

Systematic effects on the asymmetry measurement may be investigated by separating the data into two groups based on which helicity state is set first. The first group (black data points) represents the electron asymmetry observed when the first (original) helicity state is negative and its complement state is positive (helicity state #1 – state #4). The second group (red data points) represents the asymmetry observed when the first state is positive and the complement state is negative (helicity state #2 – #3). Both groups were divided into two subgroups based the target type used. The diamond points on the histogram represent the data for the NH$_3$ target and the squares for the ND$_3$ target.

70

Fig. 3.15: Run Number versus Electron Asymmetry before FC normalization. The black and red points represent reconstructed electron asymmetry for the helicity 1-4 pair for ND_3 and NH_3 target respectively. The blue and green points represent the helicity pair 2-3 for ND_3 and NH_3 respectively. The green line shows the sign of the half wave plane (HWP) and the purple line is the sign of the target polarization (TPol).

Two lines on the histogram are used to identify the sign of the half wave plate (HWP) and the target polarization (TPol). The relative spin orientation can be changed by either inserting a half wave plane (HWP) or by populating a different target polarization state with a different RF frequency. One would expect the asymmetry to change sign if either the HWP is inserted or the target polarization is rotated 180 degrees. As one can see for Figure 3.16 and Figure 3.15, the electron asymmetry (sign(hel1-hel4), sign(hel3-hel2) and sign(hel42-hel13)) changes sign if the HWP or Target Polarization sign is changed.
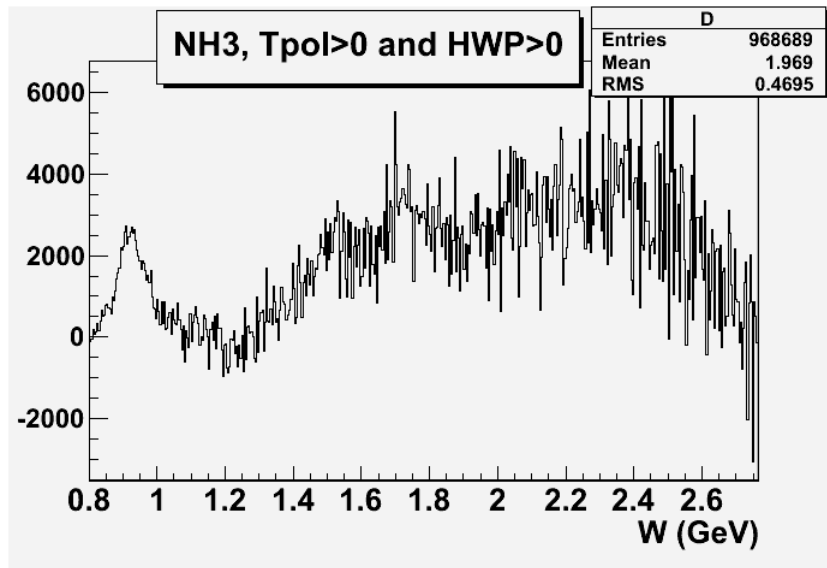
(a) NH3, Tpol>0 and HWP>0.
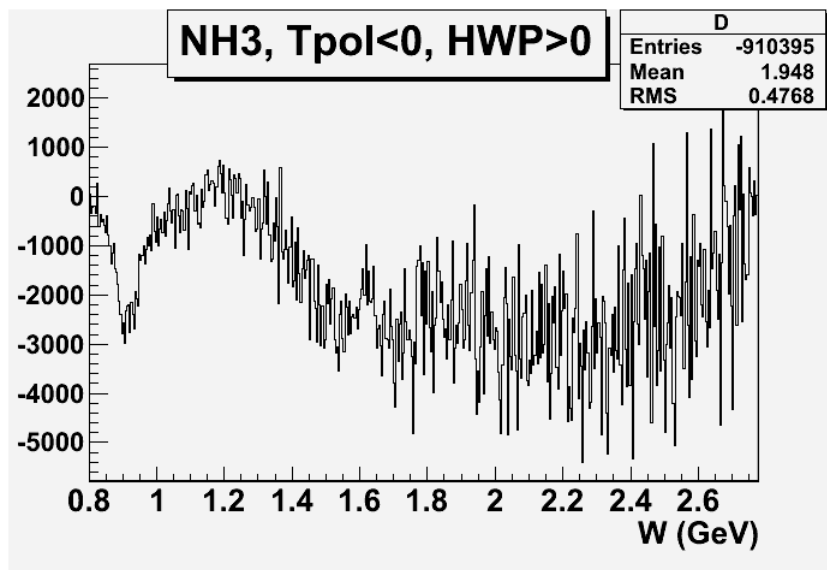
(b) NH3, Tpol<0 and HWP>0.

Fig. 3.16: W versus $(NES^{hel42} - NES^{hel13})$. The electron asymmetry (sign(hel42-hel13)) changes sign when the HWP or Target Polarization sign is changed.

The un-normalized reconstructed electron asymmetry has been calculated as:

$$A_{NES} = \frac{NES^{hel1,hel2} - NES^{hel4,hel3}}{NES^{hel1,hel2} + NES^{hel4,hel3}}, \qquad (3.24)$$

and normalized by the Faraday cup

$$A_{NES}^{FCnormalized} = \frac{\frac{NES^{hel1,hel2}}{FC^{hel1,hel2}} - \frac{NES^{hel4,hel3}}{FC^{hel4,hel3}}}{\frac{NES^{hel1,hel2}}{FC^{hel1,hel2}} + \frac{NES^{hel4,hel3}}{FC^{hel4,hel3}}}. \qquad (3.25)$$
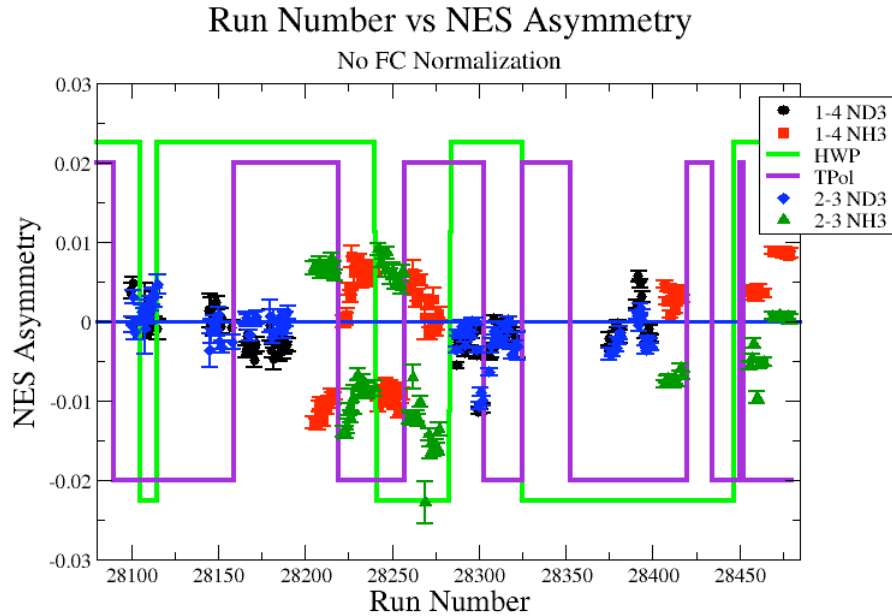

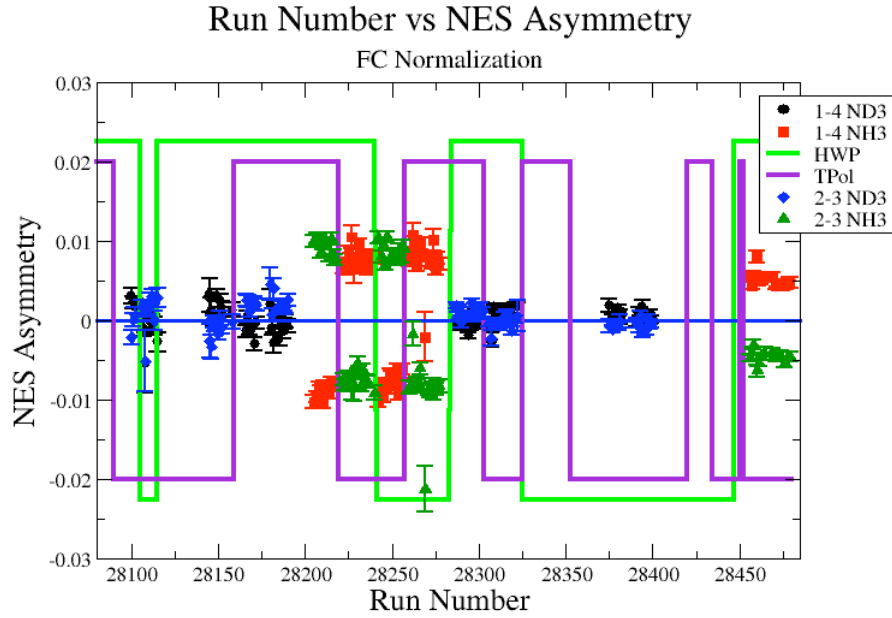Fig. 3.17: Run Number versus Electron Asymmetry after applying FC normalization. The black and red points represent the reconstructed electron asymmetry for the helicity 1-4 pair for ND_3 and NH_3 target respectively. The blue and green points are the helicity pair 2-3 for ND_3 and NH_3 respectively. The green line shows the sign of the half wave plane (HWP) and the purple line is the sign of the target polarization (TPol).

3.3.3   Semi-Inclusive Asymmetries

The asymmetries from semi-inclusive pion electroproduction using proton or deuteron targets can be written in terms of the difference of the yield when the electron spin is parallel and antiparallel to the spin of the nucleon. There are four combinations of semi-inclusive asymmetries: $A_{NH_3}^{\pi^+}$, $A_{NH_3}^{\pi^-}$, $A_{ND_3}^{\pi^+}$ and $A_{ND_3}^{\pi^-}$

$$A_{NH_3}^{\pi^+} = \frac{N_{NH_3,\pi^+}^{\uparrow\uparrow} - N_{NH_3,\pi^+}^{\uparrow\downarrow}}{N_{NH_3,\pi^+}^{\uparrow\uparrow} + N_{NH_3,\pi^+}^{\uparrow\downarrow}} \tag{3.26}$$

$$A_{NH_3}^{\pi^-} = \frac{N_{NH_3,\pi^-}^{\uparrow\uparrow} - N_{NH_3,\pi^-}^{\uparrow\downarrow}}{N_{NH_3,\pi^-}^{\uparrow\uparrow} + N_{NH_3,\pi^-}^{\uparrow\downarrow}} \tag{3.27}$$

$$A_{ND_3}^{\pi^+} = \frac{N_{ND_3,\pi^+}^{\uparrow\uparrow} - N_{ND_3,\pi^+}^{\uparrow\downarrow}}{N_{ND_3,\pi^+}^{\uparrow\uparrow} + N_{ND_3,\pi^+}^{\uparrow\downarrow}} \tag{3.28}$$

$$A_{ND_3}^{\pi^-} = \frac{N_{ND_3,\pi^-}^{\uparrow\uparrow} - N_{ND_3,\pi^-}^{\uparrow\downarrow}}{N_{ND_3,\pi^-}^{\uparrow\uparrow} + N_{ND_3,\pi^-}^{\uparrow\downarrow}}, \tag{3.29}$$

where $N_{NH_3,\pi^+,\pi^-}^{\uparrow\downarrow}$ ($N_{NH_3,\pi^+,\pi^-}^{\uparrow\uparrow}$) and $N_{ND_3,\pi^+,\pi^-}^{\uparrow\downarrow}$ ($N_{ND_3,\pi^+,\pi^-}^{\uparrow\uparrow}$) represent the number of π^+ and π^- hadrons detected in the final state with the scattered electron, when the spin of the initial electron beam was antiparallel (parallel) to the spin of the proton and neutron respectively.

The kinematic coverage for the events used in the measured asymmetries are shown on Figure 3.18 and Figure 3.19. The semi-inclusive asymmetries are listed in Table 3.3. The first group $A_{hel1-hel4}$ represents the asymmetry measured when the first original electron spin (hel1) is antiparallel to the target nucleon spin and its complement state (hel4) is parallel, whereas the second group $A_{hel2-hel3}$ represents measuring the SIDIS asymmetry when the first he-

licity state is parallel (hel2) and its complement state is antiparallel to the spin of the nucleon. For the final measurement, the two groups are combined into one $A_{hel42-hel13}$ set. Instead of looking at original and complement electron helicity states, they have been combined into the positive (hel42) and negative (he13) helicity states, which are parallel and antiparallel to the spin of the target nucleon respectively.
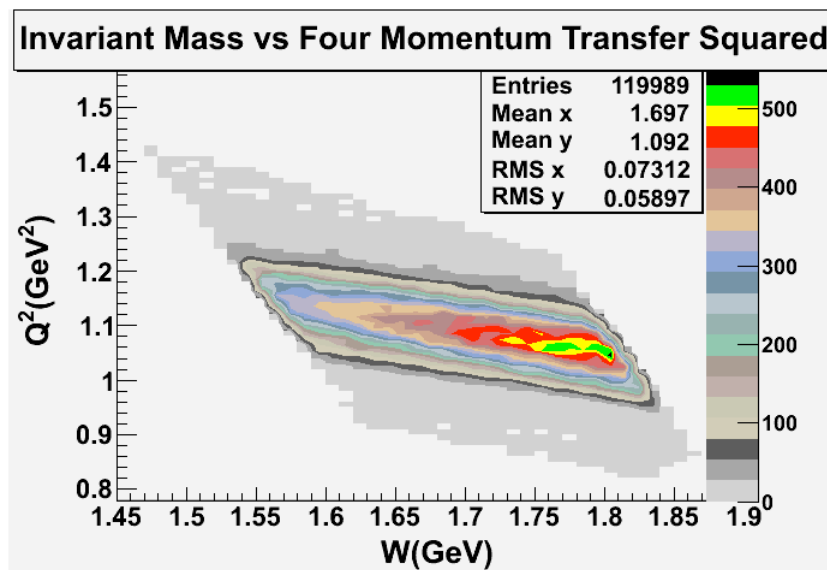
Fig. 3.18: Invariant Mass versus Q^2.

The ratio of the combined semi-inclusive deep inelastic asymmetries (A^{raw}) from Table 3.3, for two different torus settings have been corrected for the electron reconstruction efficiency. The Figure 3.20 represents the asymmetry ratios before and after electron reconstruction efficiency corrections. The ratios have been calculated for each target and charged pion type. The SIDIS asymmetries before and after the correction are statistically the same. The result indicates that the electron reconstruction efficiency does not change the asymmetries. The data have been combined for each target type and asymmetries measured
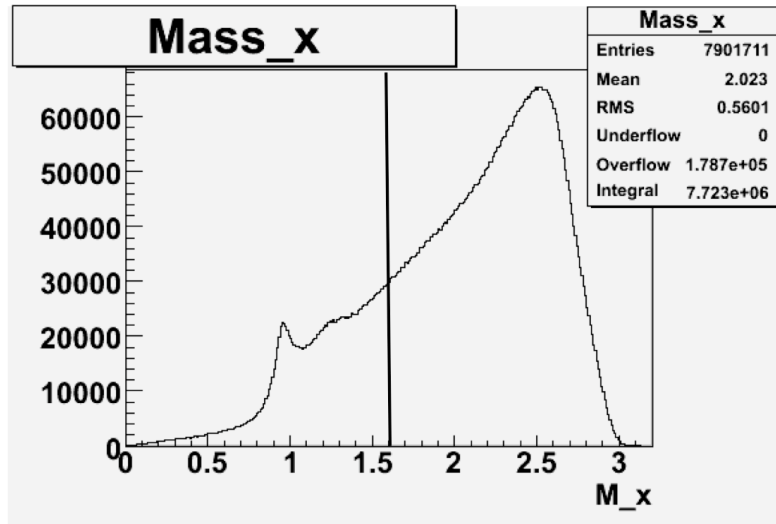
Fig. 3.19: Missing Mass.

Target type, Beam Torus	$A_{hel1-hel4} \times 10^{-4}$	$A_{hel2-hel3} \times 10^{-4}$	$A^{raw} \times 10^{-4}$
NH_3, B>0, π^+	-139.84 ± 81.52	143.15 ± 81.78	136.2 ± 57.74
NH_3, B<0, π^+	-223.76 ± 117.10	247.65 ± 116.59	237.69 ± 82.65
ND_3, B>0, π^-	-6.37 ± 188.73	-98.11 ± 188.03	9.21 ± 127.22
ND_3, B<0, π^-	-63.73 ± 105.14	-30.34 ± 6085.54	12.37 ± 71.10
NH_3, B>0, π^-	-155.45 ± 128.21	-72.55 ± 128.92	35.11 ± 90.91
NH_3, B<0, π^-	9.60 ± 119.31	72.94 ± 119.36	32.39 ± 84.38
ND_3, B>0, π^+	-76.59 ± 126.60	110.28 ± 126.13	92.25 ± 85.38
ND_3, B<0, π^+	-29.22 ± 107.53	123.98 ± 106.86	92.25 ± 85.38

Table 3.3: Run Number versus SIDIS Asymmetry for Each Type Target material and Beam Torus.

for two x_B values (Table 3.4). The SIDIS asymmetries were calculated for the following kinematic range: electron scattering angle $17.5 < \theta_e < 18.5$, electron momentum 2.55 GeV$<P_e<$2.75 GeV, invariant mass 1.6 GeV$<$W$<$1.8 GeV and momentum transferred squared 0.9 GeV$^2<Q^2<$1.3 GeV^2.

In addition to x_B, the data have been subdivided according to the fraction energy of the observed final state pion(z). $A_{NH_3}^{\pi^+,raw}$ asymmetries for two z are
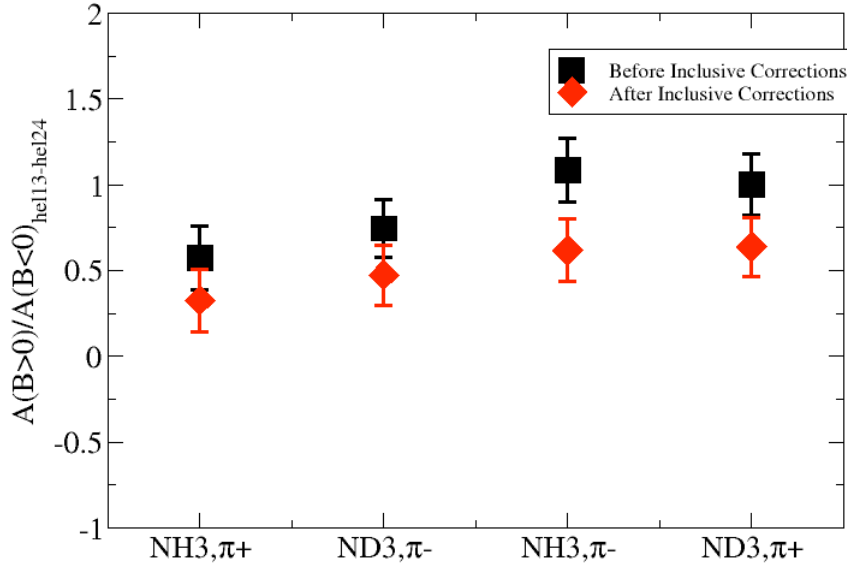
Fig. 3.20: The ratio of the SIDIS asymmetries for two torus field settings $\frac{A^{raw}(B>0)}{A^{raw}(B<0)}$ versus target and the charged pion type. The black squares represent the data before electron reconstruction efficiency and the red data - after electron reconstruction efficiency has been applied.

SIDIS Asymmetry	$x_B = 0.3$	$x_B = 0.4$
$A_{NH_3}^{\pi^+,raw}$	$(150.08 \pm 65.96) \times 10^{-4}$	$(217.20 \pm 69.06) \times 10^{-4}$
$A_{ND_3}^{\pi^-,raw}$	$(39.04 \pm 81.44) \times 10^{-4}$	$(91.90 \pm 96.14) \times 10^{-4}$
$A_{NH_3}^{\pi^-,raw}$	$(100.81 \pm 83.49) \times 10^{-4}$	$(-23.98 \pm 94.92) \times 10^{-4}$
$A_{ND_3}^{\pi^+,raw}$	$(53.17 \pm 74.89) \times 10^{-4}$	$(85.17 \pm 82.97) \times 10^{-4}$

Table 3.4: SIDIS Asymmetries for $x_B = 0.3$ and $x_B = 0.4$.

shown in Table 3.5.

z	$x_B = 0.3$	$x_B = 0.4$
0.4	$(125.62 \pm 81.92) \times 10^{-4}$	$(165.81 \pm 86.76) \times 10^{-4}$
0.7	$(140.32 \pm 158.98) \times 10^{-4}$	$(238.34 \pm 156.79) \times 10^{-4}$

Table 3.5: $A_{NH_3}^{\pi^+, raw}$ SIDIS Asymmetry.

3.3.4 Dilution Factor

To exclude the contributions of polarized nucleons from the non-hydrogen nuclei in the ammonia target (Nitrogen) and the cooling material of the target (Helium) cell to the semi-inclusive rates, the measured raw double spin asymmetries have to be divided by a dilution factor. The dilution factor accounts for the fraction of events coming from the desired polarized target nucleon. The dilution factors are calculated by combining the data from runs using different target types. During the EG1b experiment, several runs were taken with Carbon C^{12} and an empty target cell (He). All the runs in this thesis used liquid Helium as the coolant during the experiment. The Carbon and empty target runs were used to estimate the dilution of the data by the noise attributed to the interaction of the incident electron beam with the Nitrogen or Helium nucleons present in the target cell [37].

In order to calculate the dilution factor, we need to define the number of counts $N_{A,C,MT}^{hel13,hel24}$ with beam helicity negative and positive for ammonia, Carbon and empty target runs. All are weighted by the corresponding gated Faraday cup counts [38]. Normalized rates are defined as

$$n_{C,MT} = \frac{N_{C,MT}^+ + N_{C,MT}^-}{FC^+ + FC^-} \tag{3.30}$$

and

$$n_A = \frac{1}{2}\left(\frac{N_A^+}{FC^+} + \frac{N_A^-}{FC^-}\right), \qquad (3.31)$$

where n_C is the rate from a Carbon target, n_{MT} is from an empty target and n_A is from one of the NH_3 or ND_3 ammonia targets.

The counts for all four targets (empty, Carbon and ammonia) can be expressed as the sum of counts from the entrance and exit window foils (ρ_F, l_F, σ_F), liquid Helium coolant (ρ_{He}, l_{He}, σ_{He}), Carbon(ρ_C, l_C, σ_C), Nitrogen (ρ_N, l_N, σ_N), Hydrogen (Deuterium) ($\rho_{H(D)}$, $l_{H(D)}$, $\sigma_{H(D)}$).

$$n_{MT} = \rho_F l_F \sigma_F + \rho_{He} L \sigma_{He} = f\rho_C l_C \sigma_C + \rho_{He} L \sigma_{He}, \qquad (3.32)$$

$$n_C = \rho_F l_F \sigma_F + \rho_C l_C \sigma_C + \rho_{He}(L - l_C)\sigma_{He}, \qquad (3.33)$$

and

$$n_A = \rho_F l_F \sigma_F + \rho He(L - l_A)\sigma_{He} + \rho_A l_A(\sigma_N + 3\sigma_{H(D)}), \qquad (3.34)$$

where $f = \frac{\rho_F l_F \sigma_F}{\rho_C l_C \sigma_C}$, $\sigma_{H(D)}$ represents the Hydrogen (Deuteron) cross section.

Using above system of equations, we define two new spectra to account for the Carbon target and the difference in the amount of Helium in ammonia targets vice versa the Carbon target. For a target cell with length L and the Carbon target with length l_C, the Carbon and LHe contributions can be written

following way:

$$n'_{12C} = \frac{L}{L + fl_C}n_C - \frac{L - l_C}{L + fl_C}n_{MT} = \rho_C l_C \sigma_C \qquad (3.35)$$

and

$$n'_{4He} = \frac{(1 + f)l_{He}}{L + fl_C}n_{MT} - \frac{fl_{He}}{L + fl_C}n_C = \rho_{He} l_{He} \sigma_{He}, \qquad (3.36)$$

where n'_{12C} is the rate from the Carbon nucleus only and n'_{He} is the rate from liquid Helium only. The length and densities are listed in Table 3.6.

We need to establish how the rate from the Carbon target is related to the rate from the N^{15} in NH_3 and ND_3. The cross section for N^{15} can be written in terms of the cross sections on C^{12} target material (σ_{12C}) and on a bound neutron in N^{15} (σ'_n).

$$\sigma_{15N} \approx \frac{7}{6}\sigma_{12C} + \sigma'_n = \left(\frac{7}{6} + \frac{\sigma'_n}{\sigma_{12C}}\right)\sigma_{12C}. \qquad (3.37)$$

It is assumed that when the scattering occurs on protons inside the target material, the ratio of $\frac{\sigma'_n}{\sigma_{12C}} = 0$ and when the reaction happens on neutrons inside the target, the value of the ratio is $\frac{\sigma'_n}{\sigma_{12C}} = \frac{1}{6}$, because there are six bound neutrons in C^{12} [38].

Using above quantities the background represented by the number of counts due to the non-hydrogen and non-deuterium parts of the ammonia target can

be expressed as

$$
\begin{aligned}
n_B &= \left[\frac{\rho_A l_A}{\rho_C l_C} \left(\frac{7}{6} + \frac{\sigma'_n}{\sigma_{12C}} \right) + f \right] n'_{12C} + (L - l_A) n'_{4He} \\
&= n_{MT} + l_A \left[\frac{\rho_A}{\rho_C l_C} \left(\frac{7}{6} + \frac{\sigma'_n}{\sigma_{12C}} \right) n'_{12C} - n'_{4He} \right].
\end{aligned}
\tag{3.38}
$$

The dilution factor d_f is

$$
d_f = \frac{n_A - n_B}{n_A}.
\tag{3.39}
$$

The dilution factor is compared below in Table 3.8:

Item	Description	Value
$\rho_F l_F$	Density times target length for empty target.	Al: 167 μm; 0.045 g/cm^2. Kapton: 384 μm; 0.055 g/cm^2. Total=Al + Kapton=0.0996 g/cm^2
$\rho_C l_C$	Density times target length for Carbon target.	0.498 g/cm^2
f	The ratio of counts from foils to the C^{12} slab in the Carbon target.	0.200
ρ_{He}	He density.	0.145 g/cm^3
L	The length of the target cell from the entrance to exit foil.	1.90 cm
ρ_C	C^{12} density.	2.17 g/cm^3
l_C	Carbon target length.	0.23 cm
ρ_{NH_3}	NH$_3$ density	0.917 g/cm^3
ρ_{ND_3}	ND$_3$ density	1.056 g/cm^3
l_A	Ammonia target length.	0.6 cm

Table 3.6: Length and density values for different types of target material reproduced from the EG1b experiment [38].

The fractional energy of the observed final state hadron(z)	Dilution Factor(d_f)
NH$_3$, π^+ && $z = 0.4$	0.160 ± 0.02
NH$_3$, π^+ && $z = 0.7$	0.152 ± 0.03

Table 3.7: Calculated dilution Factor for NH$_3$ target type.

Reaction	Dilution Factor(d_f)
Resonance region	0.11 - 0.13
Inclusive	0.14 - 0.17
Semi-Inclusive	0.122 - 0.182

Table 3.8: Dilution Factor compared with other results [16] [37].

3.3.5 Fragmentation $\Delta R_{np}^{\pi^+ + \pi^-}$

A test of fragmentation can be performed by calculating the ratio of the difference of polarized to unpolarized cross sections for proton and neutron targets $\Delta R_{np}^{\pi^+ + \pi^-}$ and showing that it is independent of z. The fragmentation function can be written following way

$$
\begin{aligned}
\Delta R_{np}^{\pi^+ + \pi^-}(x, z, Q^2) &= \frac{\Delta\sigma_p^{\pi^+ + \pi^-} - \Delta\sigma_n^{\pi^+ + \pi^-}}{\sigma_p^{\pi^+ + \pi^-} - \sigma_n^{\pi^+ + \pi^-}} \\
&= \frac{\Delta\sigma_p^{\pi^+ + \pi^-}}{\sigma_p^{\pi^+ + \pi^-} - \sigma_n^{\pi^+ + \pi^-}} - \frac{\Delta\sigma_n^{\pi^+ + \pi^-}}{\sigma_p^{\pi^+ + \pi^-} - \sigma_n^{\pi^+ + \pi^-}} \quad (3.40) \\
&= \frac{(\Delta u + \Delta\bar{u}) - (\Delta d + \Delta\bar{d})}{(u + \bar{u}) - (d + \bar{d})}(x, Q^2) \\
&= \frac{g_1^p - g_1^n}{F_1^p - F_1^n}(x, Q^2).
\end{aligned}
$$

The left side of the fragmentation function is calculated using the measured double spin asymmetries for the ammonia targets. However, the right side can

be extracted using the model.
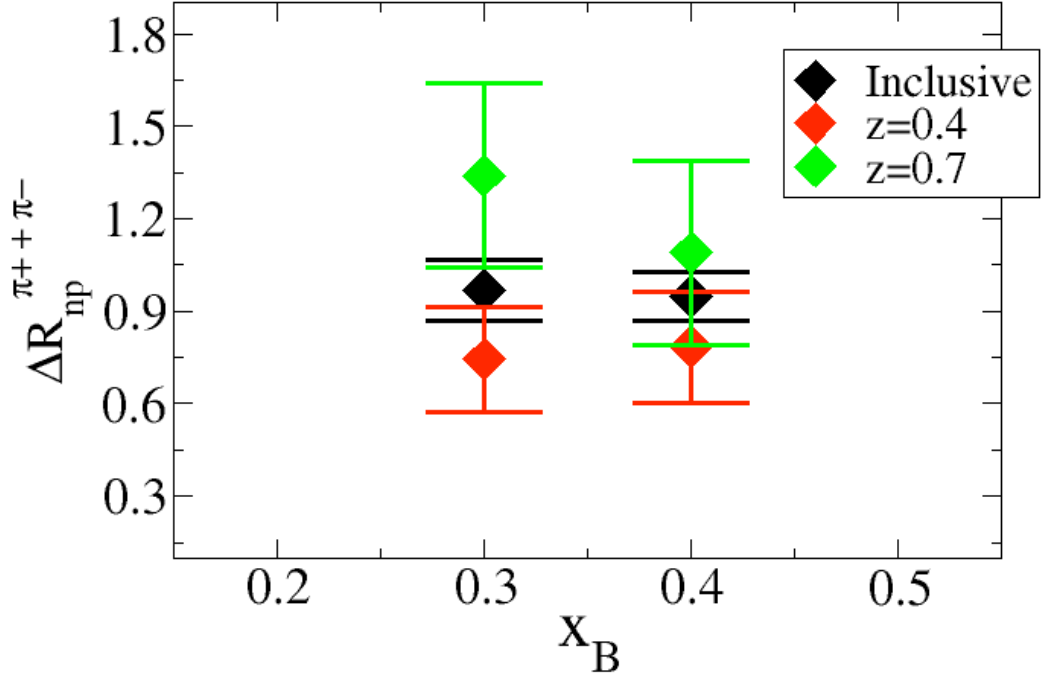
Fig. 3.21: x_B versus $\Delta R_{np}^{\pi^+ + \pi^-}$. Black data points represent the Model, red and green data points represent fragmentation function for $z = 0.4$ and $z = 0.7$ respectively.

z	$x_B = 0.3$	$x_B = 0.4$
0.4	14 %	12 %
0.7	21 %	32 %

Table 3.9: Statistical Z - test for the data comparison with the model. The probability of not observing the data point for each z and x_B values within the Inclusive Model.

The pion asymmetries, $A_{NH3}^{\pi^-}$, $A_{ND3\pi^+}$, $A_{ND3}^{\pi^-}$ are statistically consistent with

zero as shown in Table 3.4. As a result, the contributions from $\Delta\sigma_p^{\pi^-}$, $\Delta\sigma_n^{\pi^+}$ and $\Delta\sigma_n^{\pi^-}$ to the fragmentation function test (Eq. 1.54) are negligible. Only the first term is non-zero in $\Delta R_{np}^{\pi^++\pi^-}$. After correcting the cross section difference for the target polarization, beam polarization, and dilution factor, the $\Delta R_{np}^{\pi^++\pi^-}$ function for two values of z and x_B is shown on Figure 3.21 and is compared to the Model.

3.3.6 Systematic errors

Systematic errors from the experimental setup and the cuts used for particle identification and background elimination were estimated. The systematic errors associated with the electromagnetic cuts and fiducial cuts for electron identification were calculated by comparing the SIDIS asymmetries before and after cuts were applied. Systematic effects related to the dilution factor and polarization were estimated following way: First, the SIDIS asymmetries were calculated for the standard values of the dilution factor and polarization. Then asymmetries were recalculated by changing the value of the each parameter by the amount of its uncertainty. The difference between these two values is the systematic effect. The systematic errors for the SIDIS asymmetries are shown in Table 3.10.

Source	Systematic Error
Geometrical and timing cuts	5.80×10^{-2}
Electromagnetic calorimeter cut	4.07×10^{-2}
Dilution Factor	5.03×10^{-2}
Target and beam polarization	1.10×10^{-2}
Total	8.76×10^{-2}

Table 3.10: The systematic errors for the $A_{NH_3}^{\pi^+}$ asymmetry.

CHAPTER 4

Results

The final results are presented in this section. They have been obtained by analyzing the data collected in 2000 - 2001 at Thomas Jefferson National Laboratory using a longitudinally polarized electron beam on a longitudinally polarized Hydrogen ($^{15}NH_3$) and Deuterium ($^{15}ND_3$) targets. The incident electron's energy was 4.2 GeV. The CEBAF Large Acceptance Spectrometer (CLAS) was used for particle detection. The measurements were made for the kinematic region where $x_B \geq 0.3$ and momentum transferred squared between 0.9 and 1.3 GeV^2. The SIDIS asymmetries were measured for four different values of x_B. The corrected measured semi-inclusive deep inelastic asymmetries $A_{NH3}^{\pi^+}$, $A_{NH3}^{\pi^-}$, $A_{ND3}^{\pi^+}$ and $A_{ND3}^{\pi^-}$ are shown below on Figures 4.1, 4.2, 4.3 and 4.4 respectively and compared to the asymmetries measured by the HERMES experiment. The measured SIDIS asymmetries on the proton and deuterium targets are in good agreement within their combined uncertainties. The SIDIS asymmetries for longitudinally polarized Hydrogen ($^{15}NH_3$) and Deuterium ($^{15}ND_3$) targets are listed in Table 4.1 for four values of x_B. The asymmetries have been corrected for the target and beam polarization [20] and dilution factor from ref[39].

x_B	$A_{NH3}^{\pi^+} \pm stat. \pm syst.$	$A_{NH3}^{\pi^-} \pm stat. \pm syst.$
0.30	$0.1644 \pm 0.0504 \pm 0.0753$	$0.1378 \pm 0.0745 \pm 0.0751$
0.35	$0.2733 \pm 0.0400 \pm 0.0764$	$0.1183 \pm 0.0583 \pm 0.0750$
0.40	$0.3308 \pm 0.0499 \pm 0.0772$	$-0.0917 \pm 0.0753 \pm 0.0749$
0.45	$0.2521 \pm 0.1257 \pm 0.0761$	$-0.1908 \pm 0.1942 \pm 0.0755$
x_B	$A_{ND3}^{\pi^+} \pm stat. \pm syst.$	$A_{ND3}^{\pi^-} \pm stat. \pm syst.$
0.30	$0.2273 \pm 0.0317 \pm 0.0809$	$0.1286 \pm 0.0320 \pm 0.0767$
0.35	$0.0209 \pm 0.0314 \pm 0.0747$	$0.1904 \pm 0.0319 \pm 0.0791$
0.40	$0.3368 \pm 0.0322 \pm 0.0877$	$0.1080 \pm 0.0330 \pm 0.0761$
0.45	$0.2408 \pm 0.0377 \pm 0.0816$	$0.5125 \pm 0.0392 \pm 0.1024$

Table 4.1: Semi-inclusive asymmetries on the proton and deuterium targets ($A_{NH3}^{\pi^+,\pi^-}$ and $A_{ND3}^{\pi^+,\pi^-}$).
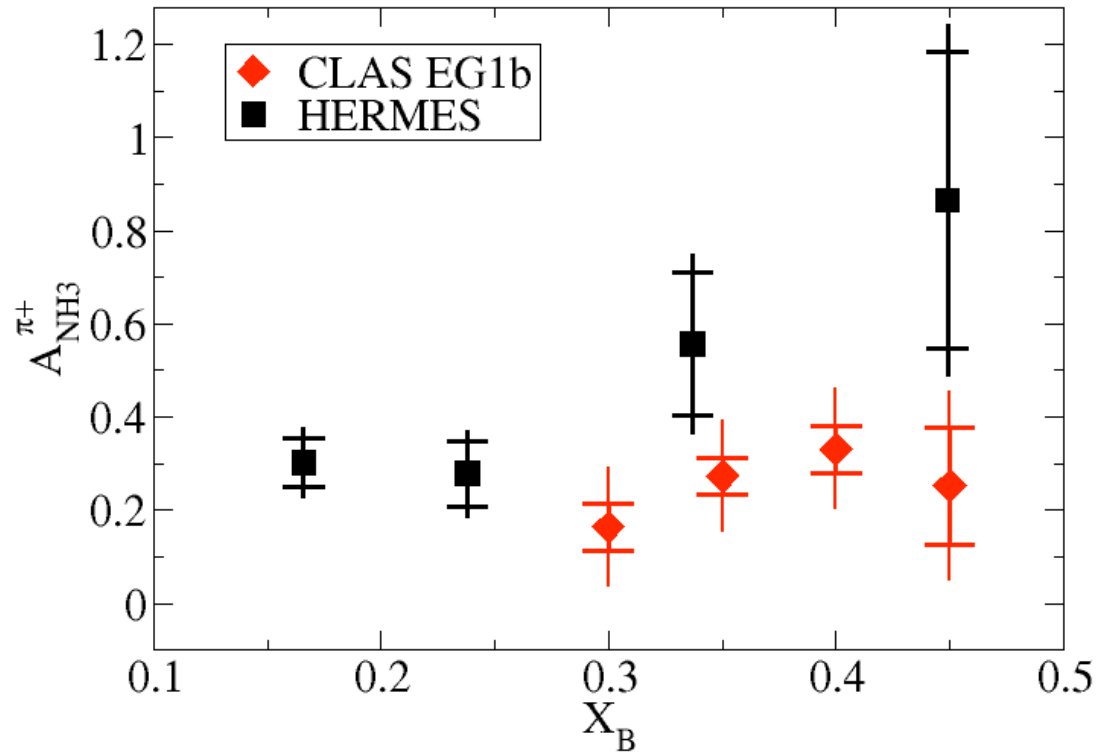
Fig. 4.1: x_B versus $A_{NH3}^{\pi^+}$ SIDIS Asymmetry. The solid black squares are measurements from ref[11] and the solid red diamonds represent SIDIS asymmetries measured using the data collected during the EG1b experiment. The error bar lines represent statistical uncertainty and the risers systematic uncertainty.

Fig. 4.2: x_B versus $A_{NH3}^{\pi^-}$ SIDIS Asymmetry. The solid black squares are measurements from ref[11] and the solid red diamonds represent SIDIS asymmetries measured using the data collected during the EG1b experiment. The error bar lines represent statistical uncertainty and the risers systematic uncertainty.
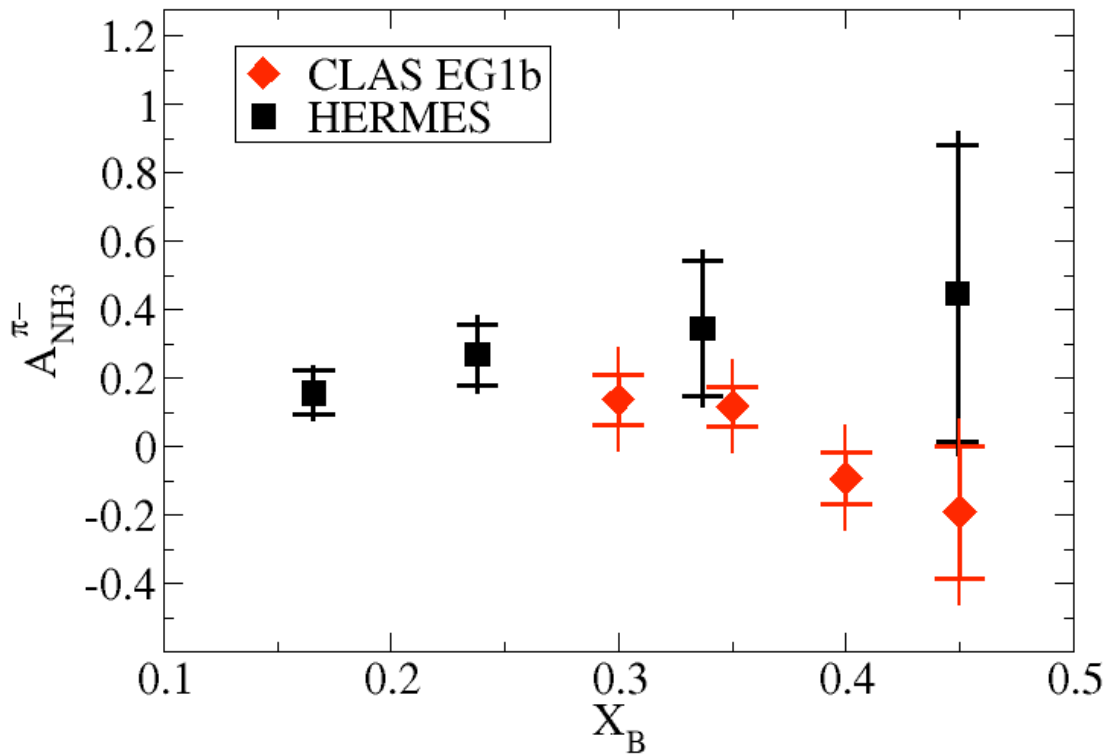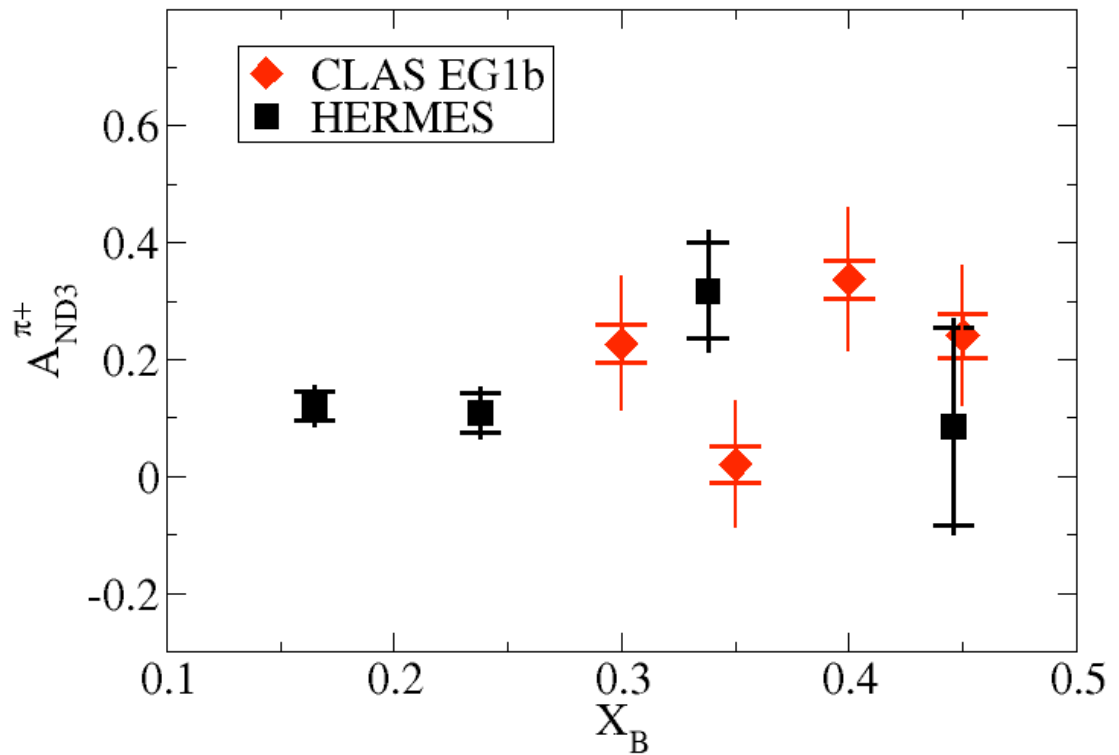
Fig. 4.3: x_B versus $A_{ND3}^{\pi^+}$ SIDIS Asymmetry. The solid black squares are measurements from ref[11] and the solid red diamonds represent SIDIS asymmetries measured using the data collected during the EG1b experiment. The error bar lines represent statistical uncertainty and the risers systematic uncertainty.

Fig. 4.4: x_B versus $A_{ND3}^{\pi^-}$ SIDIS Asymmetry. The solid black squares are measurements from ref[11] and the solid red diamonds represent SIDIS asymmetries measured using the data collected during the EG1b experiment. The error bar lines represent statistical uncertainty and the risers systematic uncertainty.
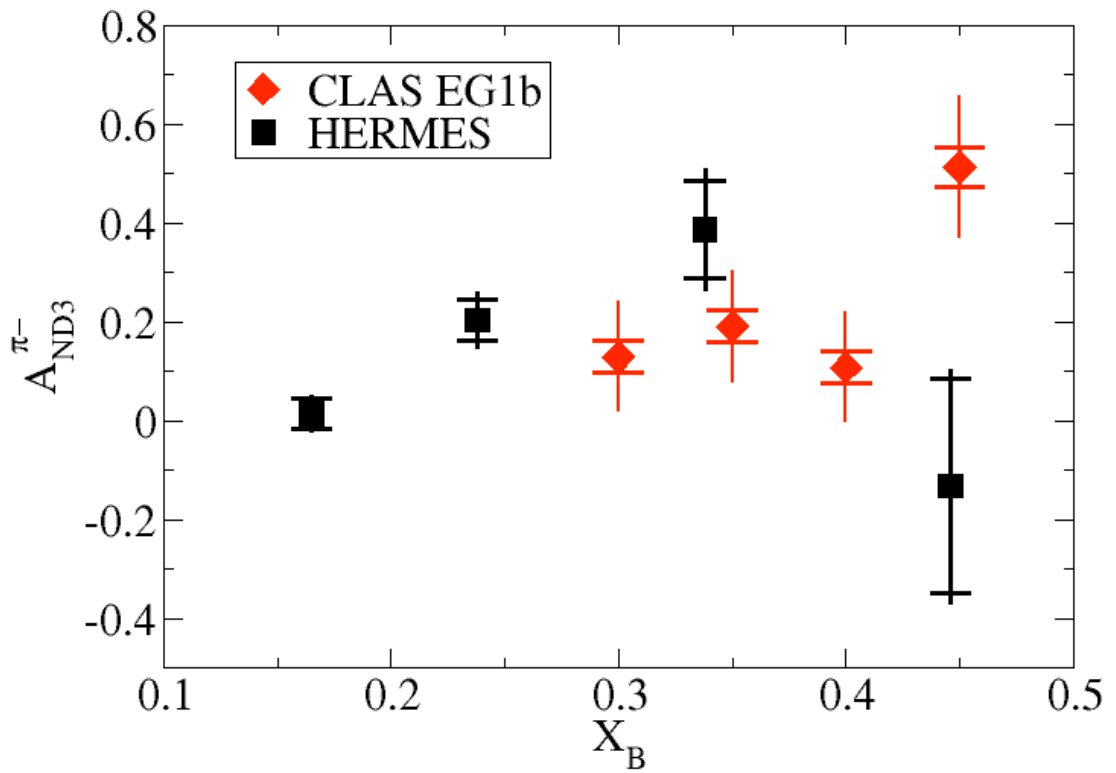
Bibliography

[1]   J. Ashman *et. al.*, (EMC Collaboration), Nucl. Phys. B**328** (1989).

[2]   J. Ashman *et. al.*, (EMC Collaboration), Nucl. Phys. B**206**, 364 - 370 (1988).

[3]   J. Ellis, and M. Karline, Phys. Lett. B**341**, pg 396 (1965).

[4]   B. Hommez. *A Study of Fragmentation Processes in the HERMES Experiments using a Ring Imaging Cherenkov Detector*. Doctoral dissertation, University of Gent, 2003.

[5]   E. Bloom *et. al.*, SLAC Group A, reported by W. K. Panofsky in *Int. Conf. on High Energy Phys., Vienna,* CERN, Geneva p.23 (1968).

[6]   F. E. Close, *An Introduction to Quarks and Patrons.* (London, UK: Academic Press Inc. LTD., 1979).

[7]   G. Dissertori, I. K. Knowles, and M. Schmelling, *Quantum Chromodynamics: High Energy Experiments and Theory.* (Oxford, UK: Oxford University Press, 2003).

[8]   R. G. Roberts, *The structure of the proton. Cambridge Monographs on Mathematical Physics.* (Cambridge, UK: Cambridge University Press, 1990).

[9]   V. V. Anisovich, M. N. Kobrinsky, J. Nyiri, and Yu. M. Shabelski, *Quark Model and High Energy Collisions.* (World Scientific Publishing Co. Pte. Ltd., 2004).

[10]   J. M. Camalich, L. S. Geng, and M. J. Vicente Vacas, *The lowest-lying baryon masses in covariant SU(3)-flavor chiral perturbation theory.* arXiv:1003.1929v1 [hep-lat] (2010).

[11]   A. Airapetian *et. al.*, (The HERMES Collaboration), Phys. Rev. Lett. 92, 012005 (2004).

[12]   E. Christova and E. Leader, *Semi-inclusive production-tests for independent fragmentation and for polarized quark densities.* hep-ph/9907265 (1999).

[13]   T. D. Averett et. al., Nucl. Instr. Meth. A**427/3**, 440-454 (1999).

[14]   D. G. Crabb and W. Meyer, Annu. Rev. Nucl. Part. Sci. **47**, 67-109 (1997).

[15]   S. Chen, *First Measurement of Deeply Virtual Compton Scattering with a Polarized Proton Target.* Doctoral dissertation, Florida State University, Tallahasee, FL, 2006.

[16]   Y. A. Prok, *Measurement of The Spin Structure Function $g_1(x, Q^2)$ of the Proton in The Resonance Region.* Doctoral dissertation. University of Virginia, Richmond, VA, 2004.

[17]   G. Baum G *et. al.*, *A proposal for a Common Muon and Proton Apparatus for Structure and spectroscopy*, CERN/SPSLC/96-14(1996).

[18]   C. D. Keith *et. al.*, Nucl. Instr. Meth. A**501**, 327-339 (2003).

[19]   V. Burkert, B. Mecking, D. Day, J. McCarthy and R. Minehart, *Polarized Target Experiments Using the CEBAF Large Acceptance Spectrometer.* CLAS - Note 90 - 04.

[20]   K. V. Dharmawardane *et. al.*, (The CLAS Collaboration), Phys. Lett. **B641**, 11 (2006).

[21]   R. H. Fatemi, *The Spin Structure of The Proton in The Resonance Region.* Doctoral dissertation, University of Virginia, Sterling, VA, 2002.

[22]   M. D. Mestayer *et. al.*, Nucl. Instr. Meth. A**449**, 81-111 (2010).

[23]   G. Adams and V. D. Burkert *et al.* (The CLAS Collaboration), Nucl. Instr. Meth. A**465**, 414-427 (2001).

[24]   E. S. Smith *et. al.*, Nucl. Instr. Meth. A**432**, 265-298 (1999).

[25]   H. A. Grunder *et. al.*, *The Continuous Electron Beam Accelerator Facility.* CEBAF-PR-87-017 (1987).

[26]   W. Diamond. *The Injector for the CEBAF cw Superconducting Linac.* CEBAF-PR-87-011 (1987).

[27]   J. Hansknecht and M. Poelker, Phys. Rev. ST Accel. Beams **9**, 063501 (2006).

[28]   D. A. Engwall *et. al.*, *A spin manipulator for electron accelerators.* CEBAF-PR-92-019 (1992).

[29]   E. Grn, E. Krger *et. al.*, Geophysical Research Lett. **24**, 2171 (1997).

[30]   B. A. Raue, L. H. Kramer, R. M. Chasteler, S. J. Gaff, J. Kelly, C. Laymon, M. Spraker, H. Weller, D. S. Carman, S. Boiarinov, V. Burkert and A. Freyberger, Bull. Am. Phys. Soc. **43**, 1543 (1998).

[31]   K. Nakamure *et. al.*, The Review of Particle Physics. Particle Data Group. J. Phys. G **37**, 075021 (2010).

[32]   M. Osipenko, A. Vlassov and M. Taiuti, *Matching between the electron candidate track and the Cherenkov counter hit.* CLAS-NOTE 2004-020 (2004).

[33]   C. Lanczos, SIAM Journal of Numerical Analysis, B**1**, 86 (1964).

[34]   K. Park, V. D. Burkert and W. Kim (The CLAS Collaboration), Phys. Rev. C**77**, 015208 (2008).

[35]   J. Pierce, *Pion Identification code,*
From EG1 Hall-B, WWW Document,
(http://www.jlab.org/Hall-B/secure/eg1/EG2000/josh/pion.cc).

[36]   Unitary Isobar Model, MAID2007, WWW Document,
(http://wwwkph.kph.uni-mainz.de/MAID//maid2007/maid2007.html).

[37]   R. G. Fersch, *Measurement of Inclusive Proton Double Spin Asymmetries and polarized Structure Functions.* Doctoral dissertation. The College of William and Mary, Williamsburg, VA (2008).

[38]   S. E. Khun, *Dilution Factor for Exclusive Channels.* Old Dominion University, Norfolk, VA (2010).

[39] P. Bosted *et. al.*, *Interpolated model calculated dilution factors for EG1b directly from radiated cross-sections*, WWW Document, (http://www.jlab.org/Hall-B/secure/eg1/EG2000/fersch/DILUTION/ dilutionmodel/) (2007).